DE-FC26-00BC15305

INTEGRATED APPROACH FOR THE PETROPHYSICAL INTERPRETATION OF POST- AND PRE-STACK 3-D SEISMIC DATA, WELL-LOG DATA, CORE DATA, GEOLOGICAL INFORMATION AND RESERVOIR PRODUCTION DATA VIA BAYESIAN STOCHASTIC INVERSION

First Annual Report for the Period

September 30, 2000 to September 30, 2001

By

Carlos Torres-Verdín

Mrinal Sen

November 2001

Work Performed under Contract No. DE-FC26-00BC15305
Prepared for U.S. Department of Energy

Dr. Purna C. Halder

Project Manager

U.S. Department of Energy
National Petroleum Technology Office
P.O. Box 3628
Tulsa, OK 74101-3628

Prepared by

The University of Texas
Center for Petroleum and Geosystems Engineering
and the Institute for Geophysics
Austin, Texas 78712

TABLE OF CONTENTS

TABLE OF FIGURES

EXECUTIVE SUMMARY

The present report summarizes the work carried out between September 30, 2001 and September 30, 2001 under DOE research contract No. DE-FC26-00BC15305.

We are glad to report that our work last year far exceeded the expectations and goals outlined in the original plan of action and proposed tasks. Communication and work interactions between UT Austin's Center for Petroleum and Geosystems Engineering and Institute for Geophysics have been both fluid and constructive. A solid working relationship between the two teams has also been established that will be most fruitful throughout the remaining stages of the project.

During the first year of work we developed a firm conceptual and software base for the project. We were also active promoting our work among US oil companies. At least two oil companies have expressed strong written interest in releasing to us comprehensive reservoir data sets to test our developments. Partial results from our work have been presented at a research workshop. We are also in the process of submitting two extended technical abstracts for conferences to take place during 2002.

This report is organized in two main sections, designated Part A and Part B, respectively. Part A details the work performed by UT Austin's Institute for Geophysics, whereas Part B summarizes the work carried out at UT Austin's Center for Petroleum and Geosystems Engineering. Work at the Institute for Geophysics centered about the development and testing of a new FORTRAN code that estimates one-dimensional distributions of P-wave velocity, S-wave velocity, and bulk density, from pre-stack seismic data. The inverse code is robust, expeditious, and efficient, and has been designed with many practical operating options in mind, including efficient τ-p transformations, adaptive regularization, and modular parallel computations. Testing of the code was successfully performed on noisy synthetic data as well as on a marine data set provided to us by UNOCAL Corporation. On the other hand, the Center for Petroleum and Geosystems Engineering developed a set of complex synthetic three-dimensional (3D) reservoir models that were subject to multi-phase fluid-flow simulation. Conversion of petrophysical parameters into elastic parameters was performed using general fluid substitution models that yielded spatial distributions of P-wave, S-wave, and bulk density. These distributions were subsequently used to simulate post- and pre-stack seismic data sets at different times during the production history of the hypothetical hydrocarbon reservoir. Inversion was applied to the simulated data sets

contaminated with 10% (or less) zero-mean Gaussian noise. The objective of such an exercise was to quantify the spatial resolution of pre- and post-stack seismic data to infer complex 3D distributions of petrophysical parameters such as porosity, fluid saturation, and pressure. A systematic inversion study showed that time-lapse 3D seismic data could at best provide a smooth spatial average of actual petrophysical properties. Complications may therefore arise in cases where the reservoir consists of thinly bedded flow units. The same study showed that pre-stack seismic data provides the most flexibility to uniquely resolve distributions of petrophysical parameters. Similarly, a study was put forth to quantify the ability of seismic data to infer petrophysical parameters in cases of loose dependency (or statistical correlation) between elastic and petrophysical parameters. As expected, the inference power of 3D seismic data becomes dramatically compromised when such a correlation is poor.

Synthesis of the work performed by both research teams consistently showed that a unique combination of wireline data and pre-stack seismic data would yield the vertical and lateral resolution needed to approach practical reservoir estimation problems. A central part of the work planned for next year contemplates the development and testing of an inversion algorithm that will synthesize the high vertical resolution of well logs and the lateral resolution of pre-stack seismic data. We also plan to continue to develop and test inversion algorithms that can be used in connection with time-lapse seismic data. Finally, we plan to integrate our algorithms for the nonlinear inversion of 3D seismic data with similar algorithms for the nonlinear inversion of petrophysical parameters based on the use of history matching and well-testing data. Testing of these algorithms will be performed on at least one comprehensive hydrocarbon reservoir data set.

A note of gratitude goes to Jason Geosystems and Schlumberger for allowing us to use their complete line of geophysical, petrophysical, and reservoir simulation software to achieve the goals of this first phase of our research project.

NUMERICAL SENSITIVITY STUDIES OF PRE-STACK 3D SEISMIC DATA AND DYNAMIC RESERVOIR BEHAVIOR, TOWARD A STOCHASTIC INVERSION OF PRE-STACK SEISMIC DATA AND WELL LOGS

PART A: INSTITUTE FOR GEOPHYSICS

1. ABSTRACT

During the period of October 1, 2000 – September 30, 2001 (the first year of the DOE contract) we were able to reach our first year project goals successfully. They include:

- Development of a robust post-stack inversion algorithm for acoustic impedance, and
- Development of a pre-stack inversion algorithm using adaptive regularization.

Although a few impedance inversion algorithms are commercially available, they have several limitations and source codes are not available. Therefore we formulated the impedance inversion as a linearized inversion algorithm with regularization and developed a fast algorithm that is robust. The algorithm has been tested on synthetic as well as field data.

A new approach to pre-stack waveform inversion scheme that uses a fast method of evaluating Fréchet derivatives and an adaptive regularization was developed and tested on synthetic and field data. Detailed descriptions of the algorithm and results from synthetic as well as field data from the Gulf of Thailand are given in the following section.

2. PRE-STACK INVERSION

Pre-stack seismic waveform inversion is a highly challenging task. The non-linearity and non-uniqueness together with compute intensive forward modeling, make the problem intractable. Here we report on a new approach to addressing these issues that make use of innovative gradient calculation, adaptive regularization, and an efficient

conjugate gradient scheme. The results from our approach are highly encouraging in that we are able to invert large dataset with nearly 600 model parameters fairly rapidly. Not only that, because of the use of adaptive regularization, we are able track smooth as well as sharp variations in the impedance, Vp and Vs (Poisson's ratio) profiles when realistic starting solutions are used. Thus our algorithm can be applied in routine analysis of large volume of seismic data. The results from the pre-stack inversion will be used in seismic reservoir characterization.

3. INTRODUCTION

Estimation of rock properties from reflection seismic data is an area of active research. Subsurface rock properties are manifested in seismic data as variations in travel times, amplitudes, and waveforms. It is well recognized that the travel times are sensitive to smooth changes (or low frequency variations) in velocity field while the amplitudes are affected by fractional or high frequency variations in elastic parameters. The normal moveout processing either in offset-time (x-t) (Taner and Koehler 1969) or plane wave (τ–p) domain (Stoffa et al. 1982) results in low frequency velocity variations (root mean square velocities in x-t and interval velocities in τ–p domain). Such low frequency velocity fields are useful for time to depth conversion, i.e., they can be used for estimating depths. However more detailed estimates of velocity field are necessary for lithology discrimination and direct detection of hydrocarbons (e.g, Castagna and Backus, 1993). This is achieved by amplitude versus offset or AVO analysis (see Castagna and Backus, 1993 for a detailed discussion), which estimates fractional changes in impedance and Poisson's ratio by least squares fitting of amplitudes on NMO corrected offset or angle gathers (Smith and Gidlow, 1987; Xia et. al., 1997) to a linearized approximation of reflection coefficient (Aki and Richards, 1980). In an AVO analysis, background velocities are used to apply normal moveout and spherical spreading corrections. These velocities are also required to transform offset gathers into angle gathers. Note, however, that the linearization of reflection coefficients is done assuming either small contrast in rock properties or small angles of propagation. Thus an AVO analysis is based on a 'primaries only' model of P wave reflection coefficient; mode-converted waves and internal multiples are not included (Simmons and Backus, 1996). Unlike the conventional

approaches, our AVO analysis (Xia et al., 1997) makes use of gathers that have been transformed from offset-time (x-t) to delay time – ray parameter (τ–p) domain. The (τ–p) domain offers the following advantages:

(a) Interval velocities can be computed by interactive velocity analysis with iterative layer stripping in a top-down fashion,

(b) A theoretically correct cylindrical slant-stack automatically corrects for spherical spreading without any requirement of background velocities,

(c) This domain naturally generalizes to more complex media such as anisotropic media, and ray-parameter is a fundamental quantity that can be used even in the analysis of multi-component data.

The AVO analysis assumes locally 1D earth model at each CMP location; normally a pre-stack time migration is applied prior to AVO to correct for lateral heterogeneity. However, results from AVO analysis and 1D waveform inversion can be erroneous if the medium is strongly laterally heterogeneous and/or anisotropic. Several of the limitations of AVO analysis can be overcome by using a more rigorous pre-stack seismic waveform inversion. In this approach synthetic seismograms are computed for an assumed earth model and compared against the data. If the fit is not acceptable, the model is perturbed, the synthetic data are regenerated and the procedure is repeated. Unlike the AVO analysis, which is a one-step procedure, the pre-stack waveform inversion is an iterative procedure. Formally, this is done by casting the model-fitting problem as an optimization procedure in which we seek an optimum earth model that honors the observations. In other words, we search for the minimum of a suitably defined error function that measures the misfit between observed and synthetic seismograms. It is now well recognized that the Pre-stack waveform inversion of seismic data is computationally demanding and complex task (Sen and Stoffa, 1991, 1992). Computational complexity arises due to the presence of (1) strong non-linearity vis-à-vis multi-modality, (2) large dimensioned system, (3) strong level of ill-posedness and (4) presence of both coherent and incoherent noises. Attempts on pre-stack inversion via least squares formalism were made (McAulay, 1985; Kormendi and Dietrich, 1991) earlier. It is widely acknowledged that gradient based minimization schemes for a nonlinear least squares problem although

provide a flexible framework, suffer substantially in robustness due to the presence of strong non-linearity and multi-modality of the objective or data misfit error functional. It thus requires a good starting model to converge to a global minimum. Recently, Xia et al. (1998) used very fast simulated annealing for full waveform inversion (Sen and Stoffa 1995). For practical applications, Xia et al. (1998) proposed a hybrid scheme in which arc-tangent parameterization was used in background velocity estimation which was then used as starting solution. However, in the final step an ad-hoc regularization was employed. Robust solutions were obtained because much care was taken to define the starting model and the search space based on travel time and AVO inversion.

In this report, we describe a new method of pre-stack inversion that is computationally efficient. Salient features of our algorithm are as follows:

- An efficient and accurate method of forward problem and Frechet derivative matrix computation,
- A robust gradient descent method in the framework of generalized least squares approach and
- Use of adaptive regularization weights during iterative minimization of error functional.

We demonstrate the applicability and usefulness of our algorithm using synthetic as well as field data.

4. FORWARD PROBLEM

Assuming that the elastic properties vary with depth only, the equation of motion and the constitutive relation can be transformed into the following system of ordinary differential equations in depth z, by applying a Fourier-Hankel transform

$$\mathbf{u} = i\omega \mathbf{A}\mathbf{u} + \mathbf{f}, \tag{1}$$

where

$\mathbf{u} = \left[u_x\, u_z\, u_y\, \tau_{xz}\, \tau_{zz}\, \tau_{yz}\right]^T = \mathbf{u}(\omega, p)$ is the stress-displacement vector that is a function of frequency ω and horizontal slowness p, $\mathbf{A}(\omega, p)$ is the system matrix that is a function of elastic coefficients and $\mathbf{f}$ is a body force term. Note that the system of ODE (Equation 1) can be derived for laterally invariant isotropic, transversely isotropic (Kennett, 1984) and

azimuthally anisotropic media (Fryer and Frazer, 1984). For isotropic and transversely isotropic media, the Eq. (1) decouples into two systems, namely a P-SV (4X4) system and an SH (2X2) system. In this paper we restrict our discussions to isotropic media only in which properties vary only in depth possessing cylindrical symmetry. The solution of the ODE (Equation 1) can be carried out by the well-known method of propagator matrices or by the unconditionally stable reflection matrix approach (Kennett, 1984). The propagation uses the eigenvalues and eigenvectors of the system matrix **A**; the eigenvalues are the vertical phase functions. For isotropic and transversely isotropic media, the eigenvector and eigenvalues of the system matrix can be derived analytically. For a general anisotropic medium, they need to be computed numerically (Fryer and Frazer, 1984). For an isotropic medium, the eigenvalues are computed using the velocity of the medium and the horizontal slowness. These eigenvalues and eigenvectors are used to define four upgoing and downgoing reflection and transmission coefficient matrices, $\mathbf{R}_D$, $\mathbf{T}_D$, $\mathbf{R}_U$, and $\mathbf{T}_U$. These are propagated through the stack of layers to obtain a composite reflection matrix that includes the effects of reflection, transmission, mode-conversion and internal multiples. Kennett (1984) derived the following iterative equation (Kennett, 1984; p.127), which can be used to compute the R/T matrices of a zone AC (**Figure A-1**) when those of zones AB and BC are known:

$$
\begin{aligned}
\mathbf{R}_D^{AC} &= \mathbf{R}_D^{AB} + \mathbf{T}_U^{AB}\mathbf{R}_D^{BC}\left[\mathbf{I}-\mathbf{R}_U^{AB}\,\mathbf{R}_D^{BC}\right]^{-1}\mathbf{T}_D^{AB} \\
\mathbf{T}_D^{AC} &= \mathbf{T}_D^{BC}\left[\mathbf{I}-\mathbf{R}_U^{AB}\,\mathbf{R}_D^{BC}\right]^{-1}\mathbf{T}_D^{AB} \\
\mathbf{R}_U^{AC} &= \mathbf{R}_U^{BC} + \mathbf{T}_D^{BC}\mathbf{R}_U^{AB}\left[\mathbf{I}-\mathbf{R}_D^{BC}\,\mathbf{R}_U^{AB}\right]^{-1}\mathbf{T}_U^{BC} \\
\mathbf{T}_U^{AC} &= \mathbf{T}_U^{AB}\left[\mathbf{I}-\mathbf{R}_D^{BC}\,\mathbf{R}_U^{AB}\right]^{-1}\mathbf{T}_U^{BC}
\end{aligned}
\qquad (2)
$$

Note that for many exploration applications, the response of an overburden region can be computed exactly in the frequency-wave number (horizontal slowness or ray parameter) domain. The response of different target zones can be computed later and combined with those of the overburden regions to obtain complete synthetic seismograms.

Note that we obtain our solution in frequency-ray parameter domain. An inverse temporal Fourier transforms results in (τ-p) seismograms. Synthetics in the offset-time domain can be obtained by plane wave synthesis of the (ω,p) or (τ-p) seismograms.

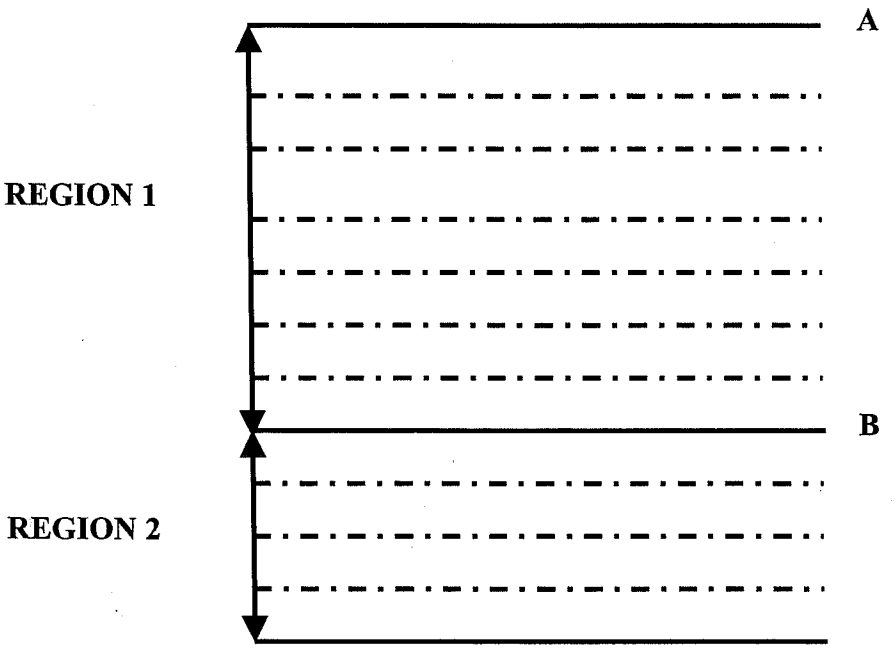

Figure A-1: A recursive scheme is used to compute the response of the zone AC, when the responses of zones AB and BC are known.

5. COMPUTATION OF GRADIENT MATRIX

In our forward modeling calculation, we compute the upward and downward looking reflection and transmission coefficient matrices of interfaces and layers in a top down fashion and use the iteration equations to compute the response of the composite media. Differential seismograms with respect to v_p, v_s and ρ can be computed by numerical differencing if seismograms for small changes in the model parameters are also computed. A brute force approach would require as many forward calculations as the total number of model parameters. This, however, is not necessary as we note that a change in one of the parameters of one layer only affects reflection/transmission through itself and through layers that are immediately above and below the current layer. One approach to achieving this is to carry out simultaneous top-down and bottom-up

reflectivity calculations and keep in memory all the intermediate R/T matrices. Once a layer parameter is perturbed, new seismograms can be generated simply by a proper combination of the pre-computed R/T matrices for top-down and bottom-up calculations. We have developed even a faster method in which we simply rearrange the R/T iteration equations and only do a top-down reflectivity calculation.

In the forward calculation, referring to **Figure A-1**, we note that given the R/T matrices of a zone AB, as we compute R/T matrices for the zone BC, we can compute the composite R/T matrices for zone AC by the iteration equations given by Equations (2). In our algorithm as we march in a top down fashion we store (or keep in memory) the composite response AC up to the current layer for each new layer that gets added in. Thus as each layer gets added in the forward computation, we have R/T matrix for the complete stack of layers (AC) and those at the base of each layer (AB). For derivative calculation, we take the following steps:

- Perturb one layer parameter, compute the R/T matrices for itself and the layers above and below it.
- Use iteration equations to compute R/T matrices from the top layer all the way to the zone right beneath the perturbed layer (New AB).
- Now we need to merge this with the R/T matrices of all the layers below it (without recomputing) to compute the complete response.

At this stage we have R/T matrices for AB and AC (old); we rearrange the iteration equations to derive an expression for R/T matrices for the zone BC. Simple algebraic manipulation results in the following expressions:

$$
\begin{aligned}
\mathbf{R}_D^{BC} &= \left(\mathbf{R}_D^{AC} - \mathbf{R}_D^{AB}\right)\left(\mathbf{T}_D^{AB}\right)^{-1}\left[\mathbf{T}_U^{AB} + \left(\mathbf{R}_D^{AC} - \mathbf{R}_D^{AB}\right)\left(\mathbf{T}_D^{AB}\right)^{-1}\mathbf{R}_U^{AB}\right]^{-1} \\
\mathbf{T}_D^{BC} &= \mathbf{T}_D^{AC}\left(\mathbf{T}_D^{AB}\right)^{-1}\left[\mathbf{I} - \mathbf{R}_U^{AB}\,\mathbf{R}_D^{BC}\right] \\
\mathbf{T}_U^{BC} &= \left[\mathbf{I} - \mathbf{R}_D^{BC}\,\mathbf{R}_U^{AB}\right]\left(\mathbf{T}_U^{AB}\right)^{-1}\mathbf{T}_U^{AC} \\
\mathbf{R}_U^{BC} &= \mathbf{R}_U^{AC} - \mathbf{T}_D^{AB}\mathbf{R}_U^{AB}\left[\mathbf{I} - \mathbf{R}_D^{BC}\,\mathbf{R}_U^{AB}\right]^{-1}\mathbf{T}_U^{BC}
\end{aligned}
\qquad (3)
$$

Thus having known the above matrices, we can use iteration equations again to compute the full response with the new perturbed model parameters. Therefore our approach is faster than brute force calculation and we do not require simultaneous top-down and bottom-up calculations either. Care, however, needs to be taken in the inversion of transmission matrices, which may, at times be nearly singular.

6. INVERSION WITH ADAPTIVE REGULARIZATION

Prestack inversion involves minimization of data misfit error between observed and computed data. If **d** is a vector of observed data, and $g(\mathbf{m})$ is the vector of computed data for some model **m** then we may define the data misfit error or error functional E_d as

$$E_d = (\mathbf{d} - g(\mathbf{m}))^T \mathbf{C}_\mathbf{d}^{-1} (\mathbf{d} - g(\mathbf{m})) . \qquad (4)$$

The suffix T denotes the transpose of the vector or matrix. $\mathbf{C_d}$ is the data covariance matrix, which is usually responsible for weighting data suitably if there is any possible noise contamination in the data. Minimization of error functional E_d is a non-trivial problem. This is due to the fact that E_d possesses strong nonlinearity vis-à-vis multimodality in general. An ordinary gradient descent type algorithm to minimize such functional often renders sub-optimality due to the presence of local minima. However, the situation improves considerably if we are able to design an algorithm where instead of minimizing the error functional defined in Eq. (4), we minimize a smooth variant of it whose smoothness is controlled adaptively. We thus define a smooth functional as

$$S(\mathbf{m};\alpha) = E_d + \alpha (\mathbf{m} - \mathbf{m}_{pri})^T \mathbf{C}_\mathbf{m}^{-1} (\mathbf{m} - \mathbf{m}_{pri}) \quad , \qquad (5)$$

where $\mathbf{m}_{pri}$ is the *a priori* model, $\mathbf{C_m}$ is the model covariance matrix and α is the regularizing weight, which plays a central role in the algorithm. Note that as α approaches zero, the smooth functional $S(\mathbf{m};\ \alpha)$ approaches the error functional E_d. The model covariance matrix may be designed to act as a smoothness operator. Here we take the following strategy; *we minimize $S(\mathbf{m},\ \alpha)$ via nonlinear conjugate gradient technique to get model update vector $\Delta\mathbf{m}^\alpha$ corresponding to each α value where* the regularization weight is obtained via modified discrepancy principle of Engl (1987). The formula that we use in determining α is given by

$$\left\| G^T G \Delta \mathbf{m}^{\alpha} - G^T \mathbf{u} \right\|_2^2 = \delta^a \alpha^{-b}, \tag{6}$$

where, G is the Jacobian matrix, $\mathbf{u}$ is the vector of data residual between observed and computed data, δ is a small value denoting noise level in data, a and b are two arbitrary constants whose values are chosen suitably with the following constraint

$$\frac{3}{2}a - 2 = b > 1 \quad . \tag{7}$$

7. NUMERICAL RESULTS

We have tested our inversion algorithm on three synthetic models. Our first example is a staircase type four-layer model (**Figure A-2**). In this model the first layer is 200 ms thick water layer, the second layer comprises low gradient for v_p, v_s and density, the third layer is characterized by a steep gradient for v_p, v_s and density and the fourth layer is a half space. For such a model, we generated synthetic τ-p gather (**Figure A-2**) with horizontal slowness ranging from 0-0.3 s/km. We used a zero phase Ricker wavelet with a peak frequency of 30 Hz for the source function. Since in most practical problems it is difficult to identify the layer interfaces from seismograms, we assume that the model consists of 229 layers with two way time of 4 ms each, in our inversion. We use a realistic smooth velocity model as a staring model (**Figure A-2**). The inverted model is compared with the starting and true models in **Figure A-2**. The reconstructed profiles for all three parameters v_p, v_s and density are in good agreement with the actual profiles. Note that the reconstructed profile for v_p is much better resolved than those of v_s and density. The scheme is able to reconstruct the impedances the best. We notice that P-wave impedance is better resolved than that of S-wave. The best-fit τ-p gather is also plotted on the adjacent panel of the **Figure A-3**. The data generated by the reconstructed model are in excellent agreement with those of the actual model.

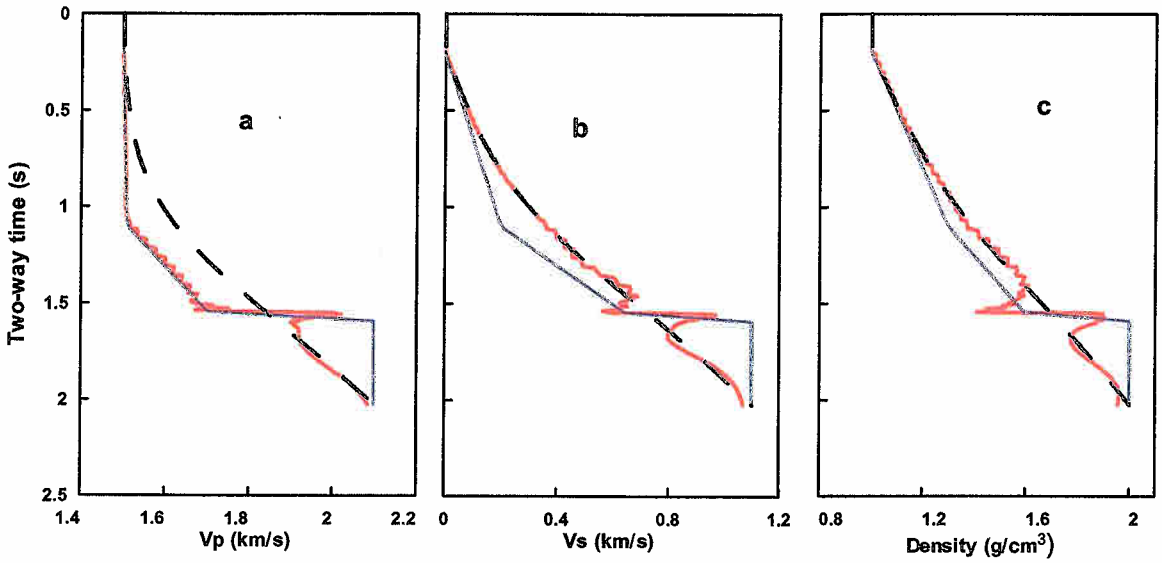

Figure A-2 (a), (b) and (c) are profiles for Vp, Vs, density vs. two-way time. Fine solid line is the true model, heavy broken line is the starting model and heavy solid line is the reconstructed profile.

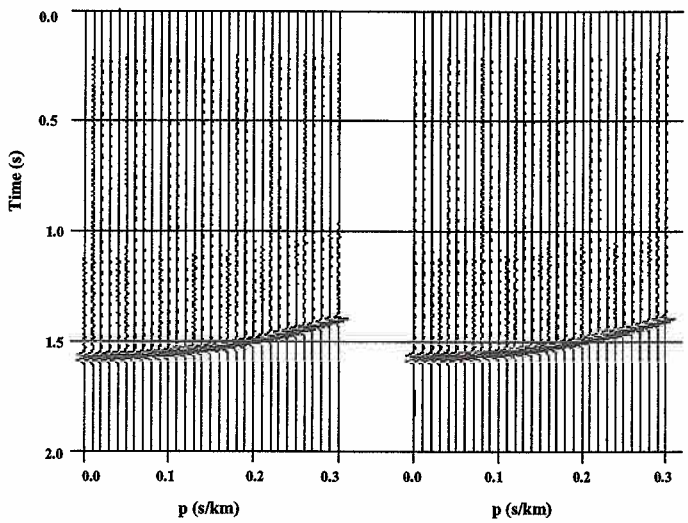

Figure A-3. τ-p gathers for (a) actual model, (b) inverted model shown in Figure A-2.

Our next example uses a model derived from a well log. The profiles of P- and S-velocity and density are presented in **Figure A-4**. For having a better clarity near anomalous zone we present a zoomed version of **Figure A-4** (**Figure A-5**). We generated

synthetic τ-p gathers with a sampling interval of 4 ms in the horizontal slowness ranging from 0-0.3 s/km using this model (Figure A-6). Once again we discretize the model with fine layers of two way time of 4 ms each. Thus our model consists of 154 layers having 462 model parameters. Inversion algorithm starts off from a smooth model (Figure A-4); the reconstructed profiles after inversion (Figure A-4) are in excellent agreement with the actual profiles. The best-fit τ-p gather is also plotted in the adjacent panel of Figure A-6. We observe that in both the examples although there are overall good agreement between the actual and the reconstructed profiles, the v_p and impedance are better resolved than the v_s profile. The fact is well understood as our data contain very little information on the low-frequency component of the shear wave profile.

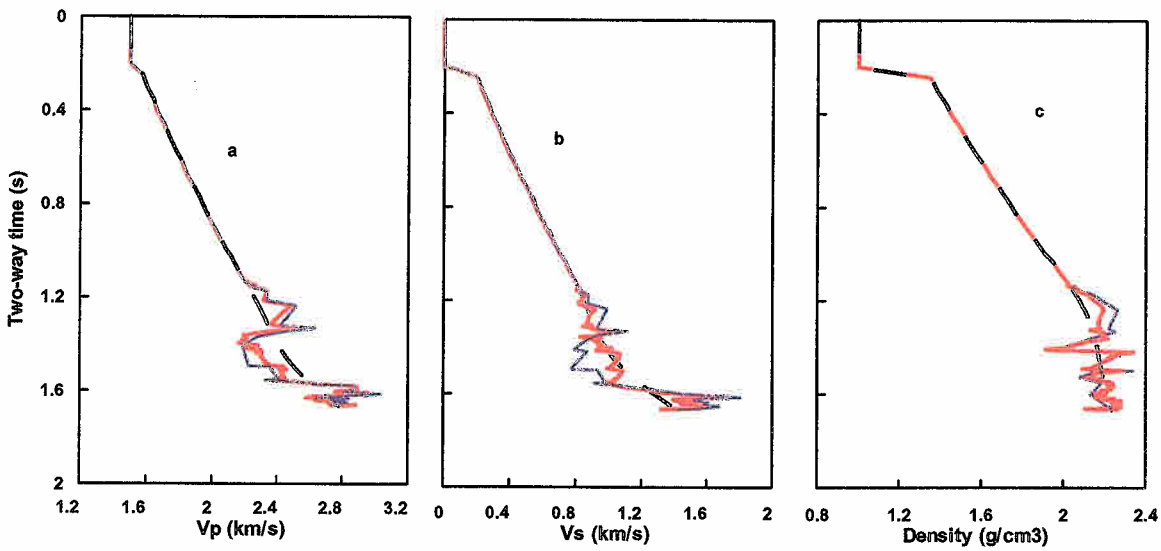

Figure A-4. (a), (b), (c) and (d) are profiles for Vp, Vs, density vs. two-way time. Fine solid line is actual, heavy broken line is a rough estimate and heavy solid line is reconstructed profile.

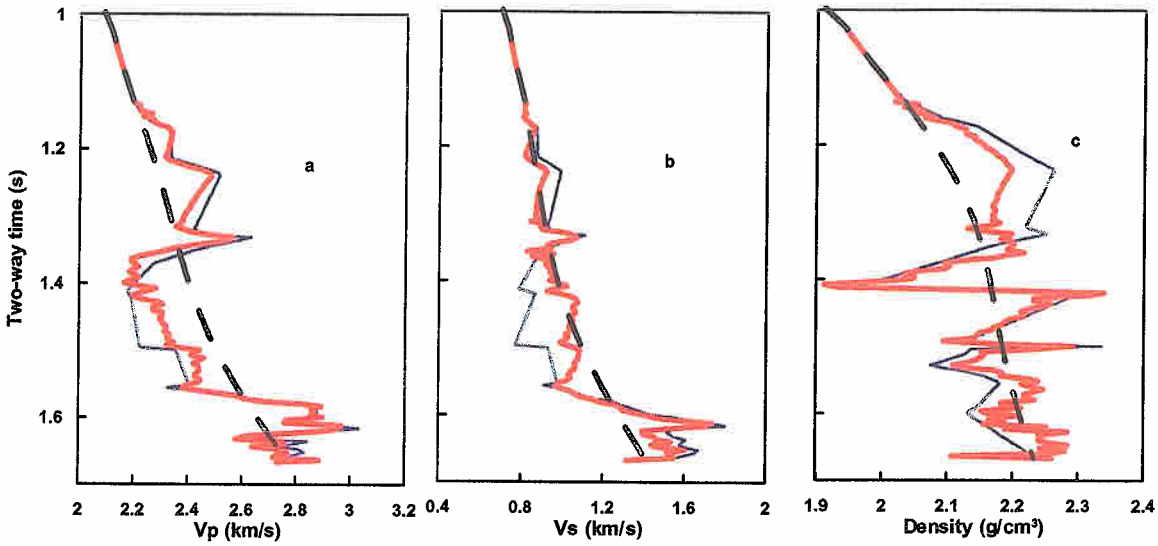

Figure A-5. (a), (b), (c) are the zoomed version of the **Figure A-4**

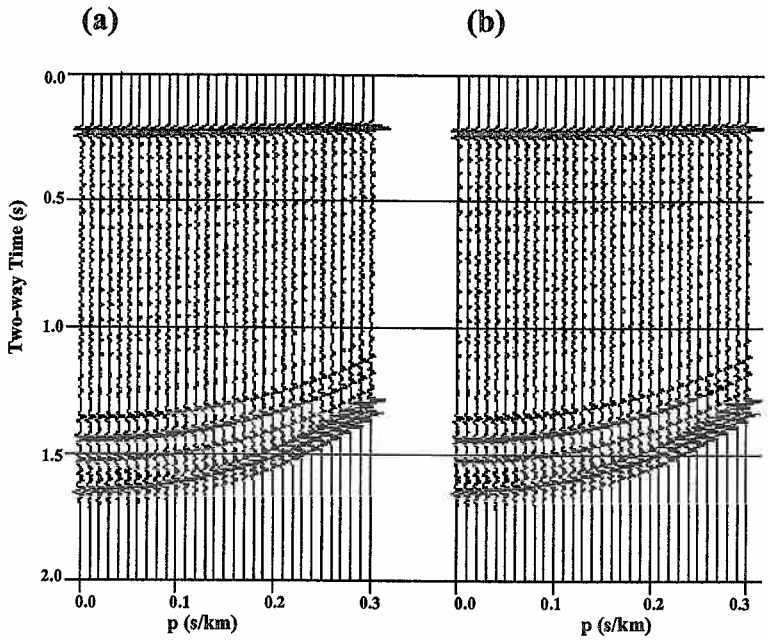

Figure A-6. τ-p gathers for (a) actual model, (b) inverted model shown in Fig A-4.

7.1 Synthetic Example No. 3.

We generated synthetic τ-p gathers for 200x200 locations for a reservoir model built by Verdin and Varela. Pre-stack inversions were performed along a complete 2D line and

at some other selected locations. The results are highly encouraging. As an example we include some of the results from that synthetic example. 2D cross-sections for different constant p-sections are shown in **Figure A-7**. The target zone (oil sand) can be clearly identified in the constant p-section. Pre-stack inversion was carried out successfully in the entire 3D volume. As an example, we include results from waveform inversion at one of the surface locations (**Figure A-8**). We used a smooth model as a starting model. The data fitting is excellent; we are able to retrieve all the important features of the model. Note that although the contrasts in shear velocity are recovered well, we are unable to reconstruct the true shear wave velocity at certain depths. This is caused by the fact that the P wave data used in the inversion does not carry information on the low frequency trend of the shear profile. This can be achieved either by using converted wave data or including well logs as priors in our inversion.

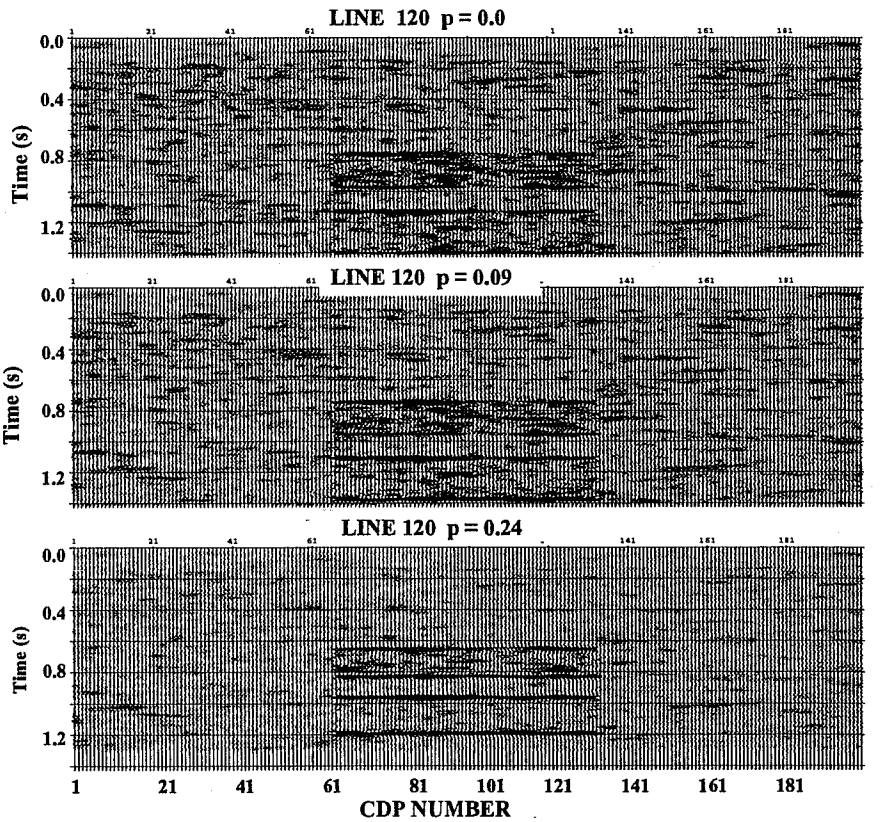

Figure A-7. Constant ray-parameter sections (2D section over the target zone) from the 3D synthetic reservoir model: the data were simulated using a tau-p modeling algorithm.

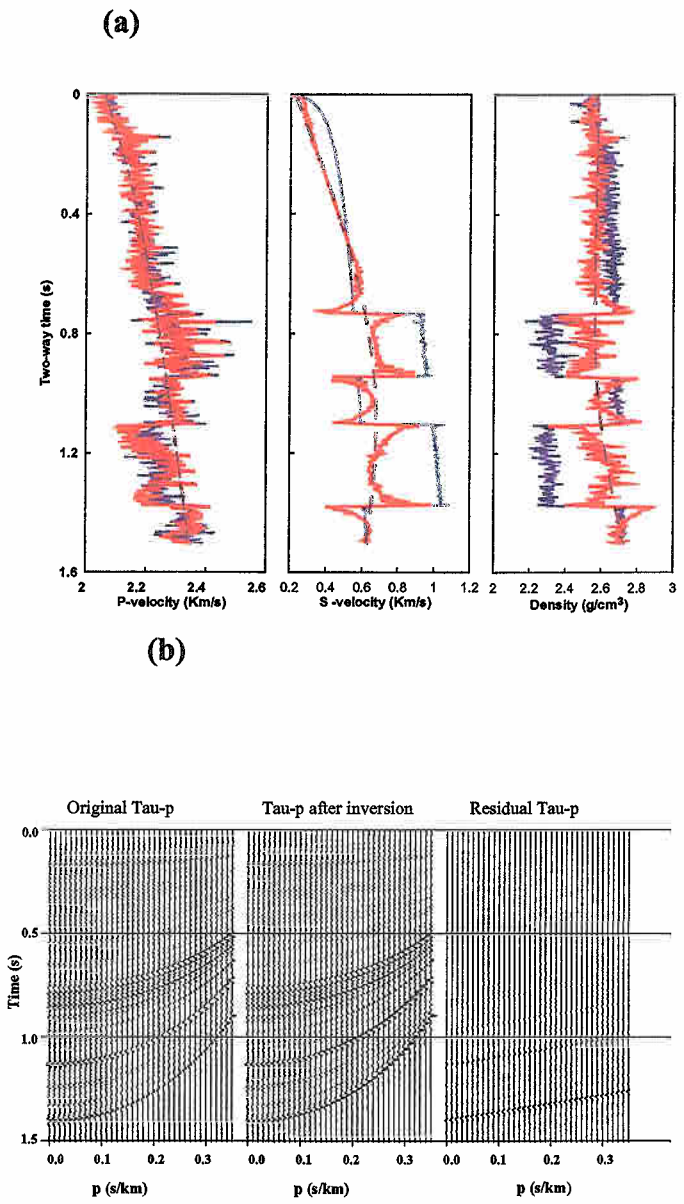

Figure A-8: Example of pre-stack tau-p inversion: the upper panel shows the starting model, true model and reconstructed model. The lower panel shows the data used in the inversion and the residual.

7.2. Gulf of Thailand Data Example

The case study area is a gas field located in the Pattani Basin, Gulf of Thailand (**Figure A-9**). The Pattani Basin is the largest and the most prolific of the basins in the Gulf of Thailand. It is located in the central portion of the Gulf, approximately 300 km long and 50 to 80 km wide. The basin fills are Tertiary non-marine and marginal marine

siliciclastic sediments shed from adjoining highlands to the north, east, and west, reaching a maximum thickness of 6000m (~20,000 ft).

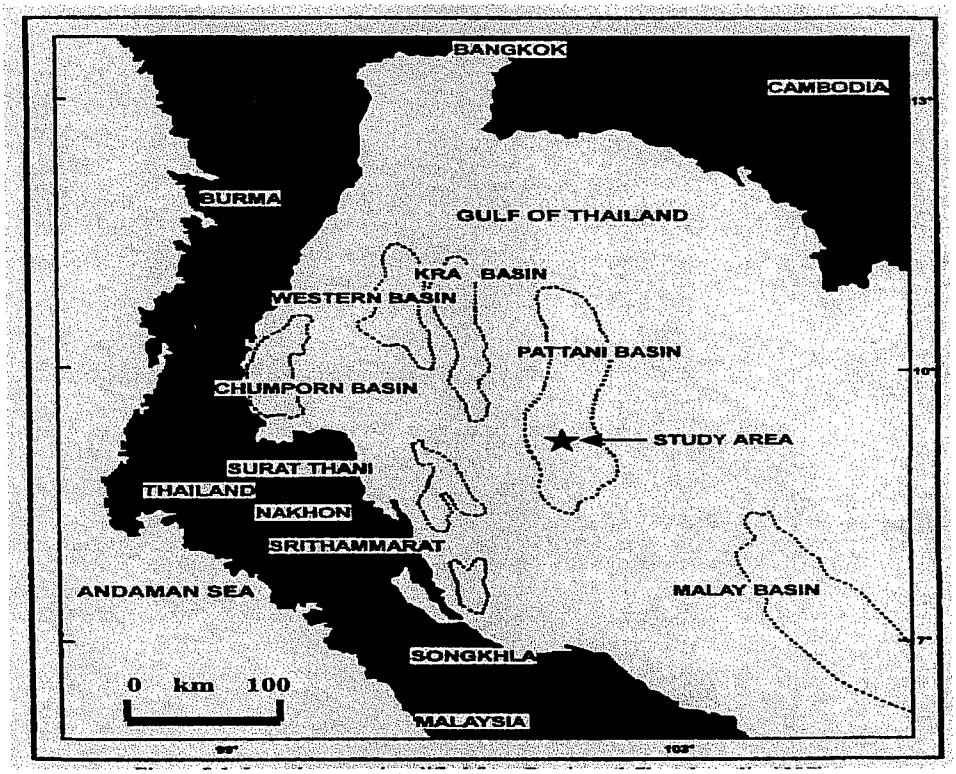

Figure A-9. Location Map: The Pattani Basin, Thailand (our study area) is shown by a star

The Unocal scientists working in the Thailand area divide the local Tertiary geologic section of the Pattani Basin into five sequences. Sequences were deposited during different stages of the structural evolution of the Pattani region. In contrast, Bustin and Chonchwalit (1995, 1997) divided the Tertiary succession into 6 units. The stratigraphy is shown in **Figure A-10**. Known reservoirs in Pattani Basin occur in any of sequence I to IV. Although thin and without strong lateral continuity, these reservoirs have good quality with porosity values ranging from 10% to 25% and most permeabilities ranging from 1 to 2000 md. These make the Pattani Basin a petroleum province with several large gas fields. In our study area, Sequence IV is the primary gas reservoir. That is, the reservoir zone lies within the time window of 1.0-2.0 sec.

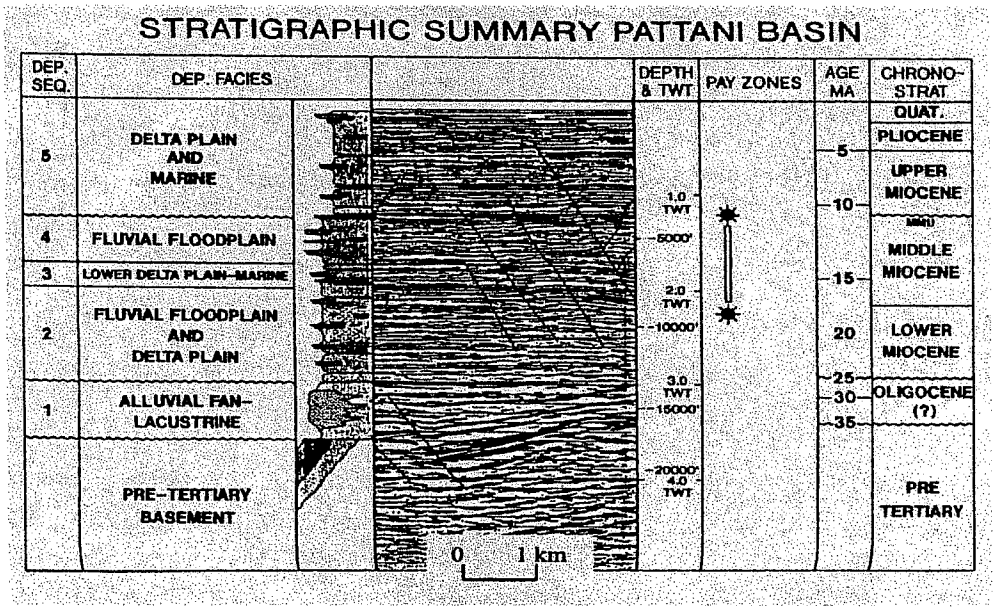

Figure A-10. Stratigraphic summary of Pattani Basin

Unocal provided us with a 2D line (Line 4) from an OBC survey (**location of the line is confidential**). During data acquisition, the source vessel shot into the seabed array in a split-spread mode to give maximum offset on both sides of the receiver. Although four components (hydrophone, vertical and two horizontal geophones) were recorded on the seafloor we only analyzed the processed hydrophone data that was combined with vertical geophone data to attenuate free surface multiples. The recording sample rate is 2 ms and the record length is 8 sec. We were provided with the processed CMP gathers (processing was done by Geco-Prakla). We carried out extensive velocity analysis and plane wave transformation of the CMP gathers. Amplitude calibration was done with synthetic seismograms for a well log. We were unable to use the well log in our inversion (except for deriving a low-frequency starting model) since the location of the well was not given and the well is a deviated one.

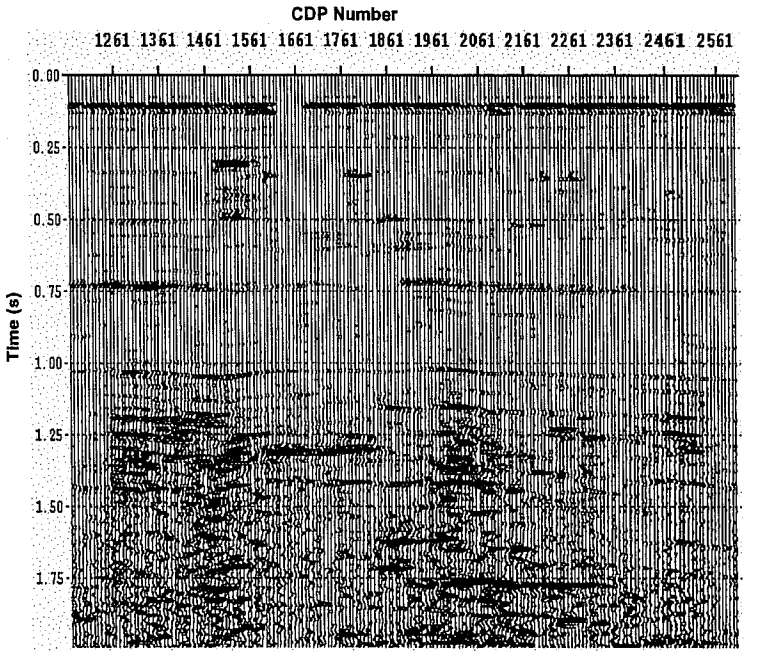

Figure A-11. Migrated stack section (P+Z component)

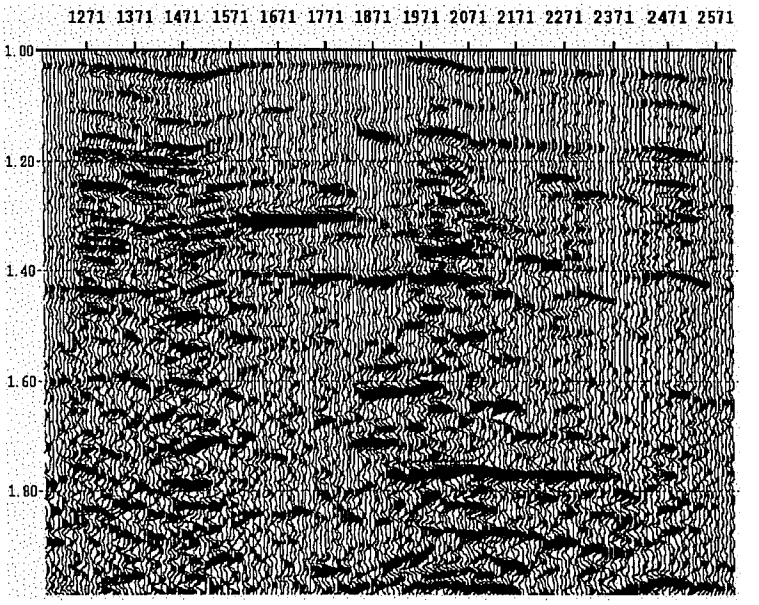

Figure A-12 Zoomed version of **Figure** A-11

Figure A-11 displays a time migrated stack section; a zoomed plot of the target zone is shown in **Figure A-12**. Note the bright reflection event at around 1.8 sec beneath CMP 1871-2271.

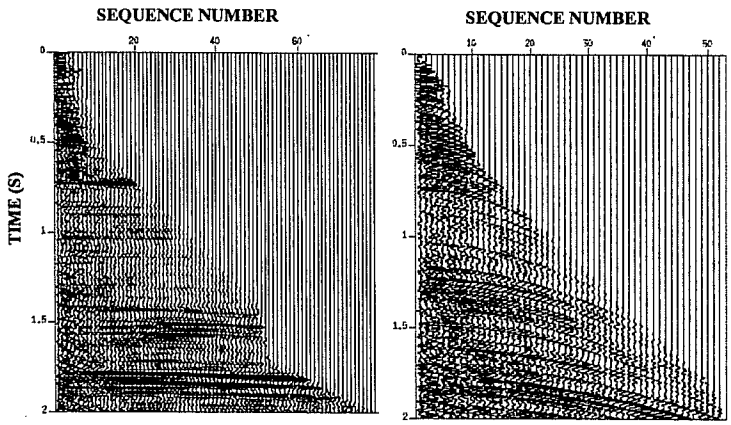

Figure A-13. Time migrated CMP-2215 gather with and without NMO

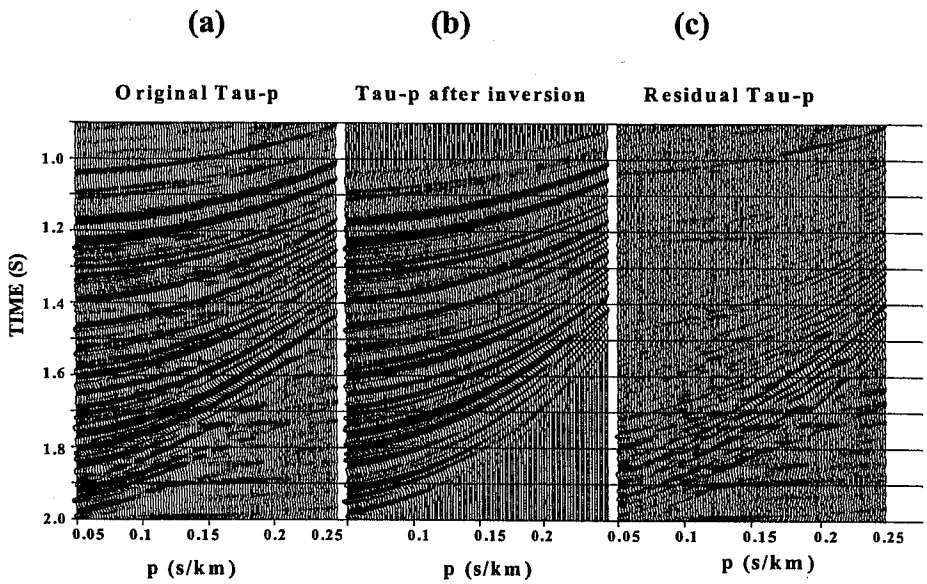

Figure A-14 (a) tau-p transformed gathers of original data, (b) data predicted by best fitting model after inversion, (c) data residual between observed and predicted data.

Figure A-14 (a) shows the tau-p transformed gathers; **(b)** is the data predicted by the best fitting model obtained by our prestack inversion. The NMO corrected tau-p gather, synthetics for the best-fit model and the residual are shown in **Figure A-15**.

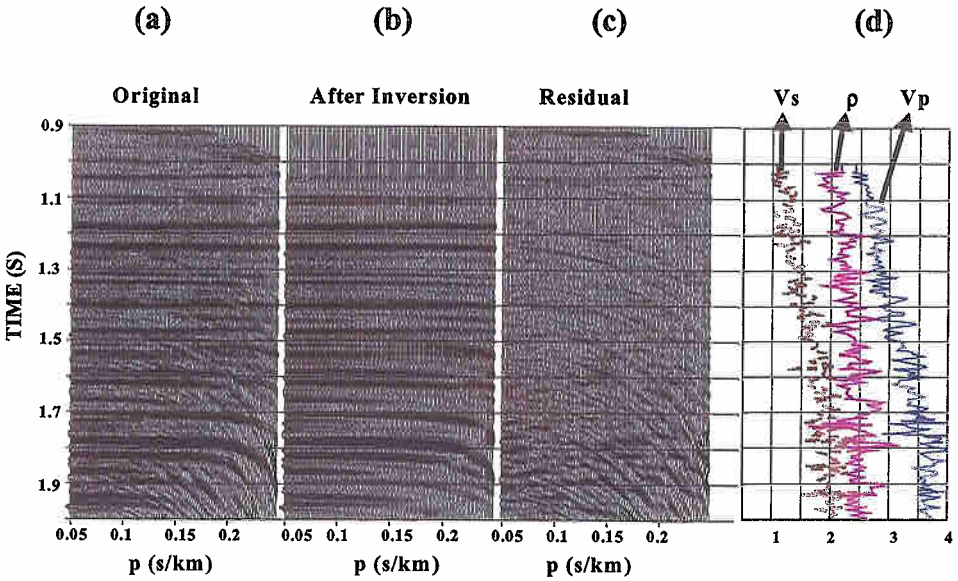

Figure A-15 (a) NMO corrected tau-p transformed of original data, (b) data predicted by best fitting model after inversion, (c) data residual between observed and predicted data, (d) derived Vp,Vs and density profiles.

The derived model for this CMP including impedance and Poisson's ratio profiles is shown in **Figure A-16**.

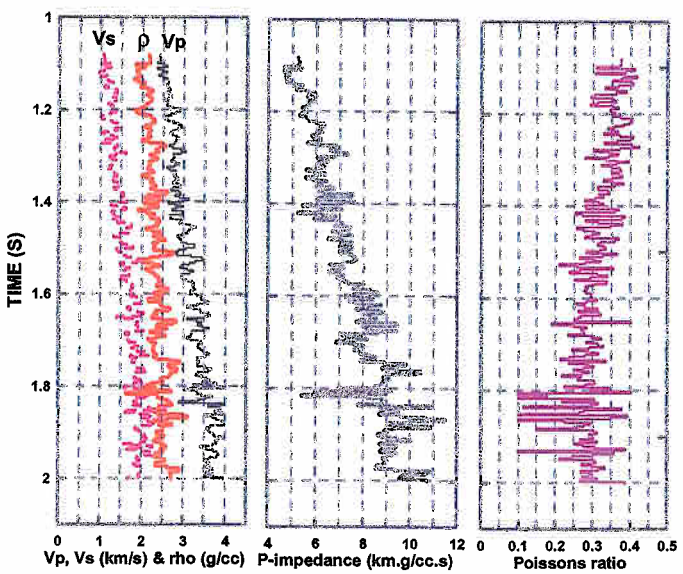

Figure A-16 Derived profiles for (a) Vp, Vs and density; (b) P-impedance and (c) Poisson's ratio.

Note that around 1.7 s we predict a zone of negative impedance and low Poisson's ratio indicating gas layer. Inverted results for three CMP locations are plotted on the stack section in **Figures A-17**.

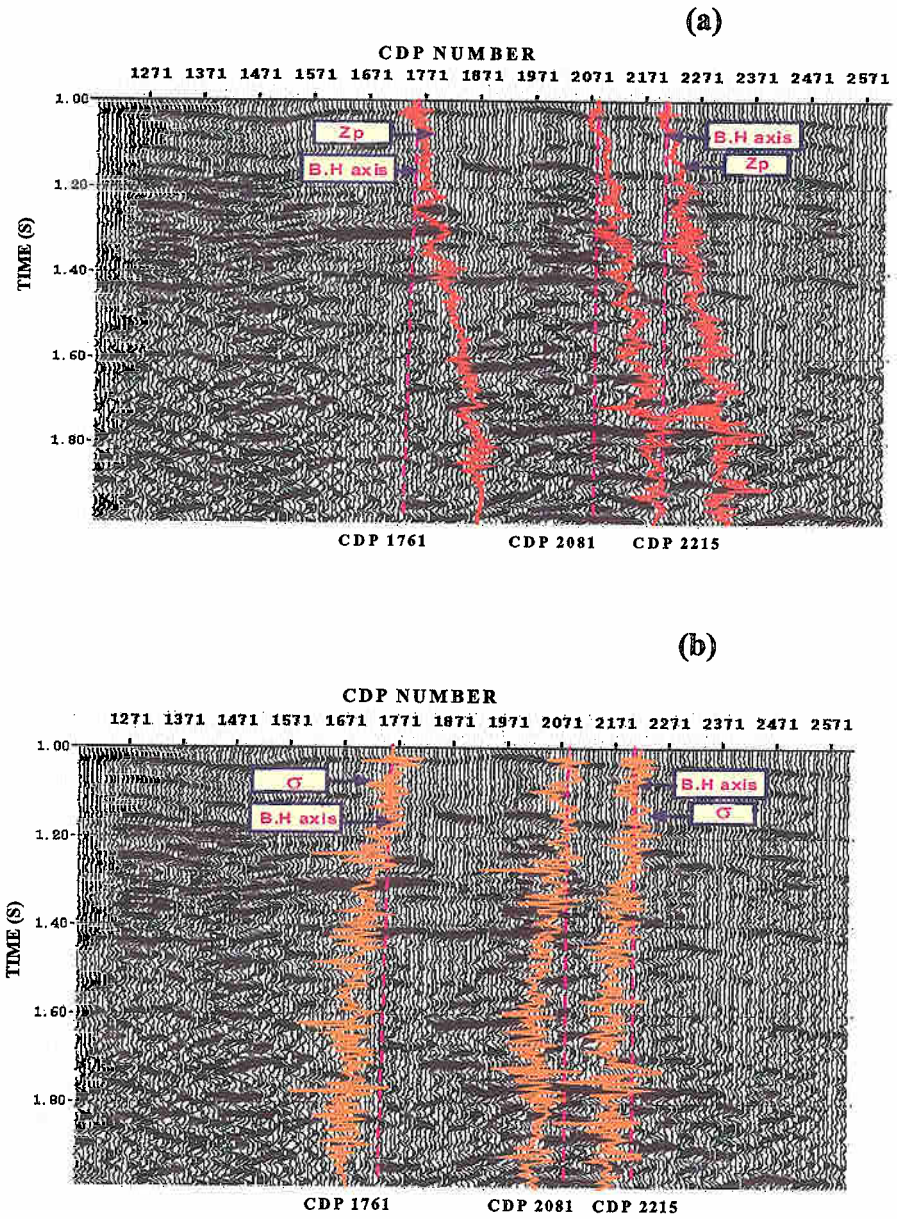

Figure A-17 (a) P-impedance and (b) Poisson's ratio profiles for three CDP locations (CDP-1761, 2081 and 2215) are overlain on the migrated stack section.

8. SUMMARY OF PART A

We have developed a pre-stack seismic data inversion in τ-p domain based on a gradient-type optimization scheme. In this method, a smooth functional is minimized using a nonlinear conjugate gradient technique to determine model update corresponding to each adaptively determined regularization weight. The algorithm is able to reconstruct the model parameters both for discrete and continuum models reasonably well. The algorithm is found to be efficient in that we were able to successfully invert both synthetic and field seismic data. We are currently implementing the code on a cluster of PCs using MPI message passing.

PART B: CENTER FOR PETROLEUM AND GEOSYSTEMS ENGINEERING

1. ABSTRACT

The ultimate goal of this project is to develop a novel strategy for the static and dynamic characterization of hydrocarbon reservoirs. This strategy is based on the extensive and effective use of 3D seismic data, wireline logs, core data, geological information, and production history data. A stochastic simulation procedure will be used to extrapolate petrophysical variables laterally away from the wells subject to honoring the existing 3D seismic data in a direct and accurate fashion. The benefit of this data integration is the generation of a more accurate reservoir model that can be used for reservoir surveillance and management.

Using inversion, a numerical sensitivity study and analysis of dynamic seismic measurements were performed in order to understand the relationships among the petrophysical and elastic parameters. We also quantified the spatial resolution of post- and pre-stack 3D seismic when estimating dynamic reservoir changes due to production. The main results show that multiphase fluid-flow parameters have a significant impact on fluid saturation, pressure distributions, and elastic parameters. Seismic data, at best, provide a smooth spatial average of pressure and fluid saturation distributions. Also, pre-stack inversion has significantly more information than post-stack acoustic impedance and this suggests that we can reliably quantify rock and fluid properties from pre-stack seismic data.

2. INTRODUCTION

The purpose of reservoir characterization is to construct a geological model with properties described by measurable petrophysical or geological parameters (i.e. lithology, porosity, permeability, etc.) making use of seismic data (i.e. travel times, amplitudes) and any additional knowledge available (i.e. well log information, core samples, geological interpretation). Here we will focus on constructing a synthetic reservoir model to test and quantify the ability of different measurements to describe the static and dynamic behavior of hydrocarbon reservoirs. We also quantify the spatial resolution of post- and pre-stack 3D seismic data to estimate dynamic reservoir changes due to production. For this

purpose we model a water-flood process, generate seismic data by means of rock physics models, and use pre-stack and post-stack seismic data for seismic inversion in an attempt to identify both lithology and pore fluids. The use of 3D seismic data is widely recognized among reservoir practitioners, especially at the stage of deriving a geometrical model of reservoir compartments and estimating their vertical and lateral continuity. The inversion techniques of seismic amplitudes have also proved to be of great practical value (**Figure B-2.1**).

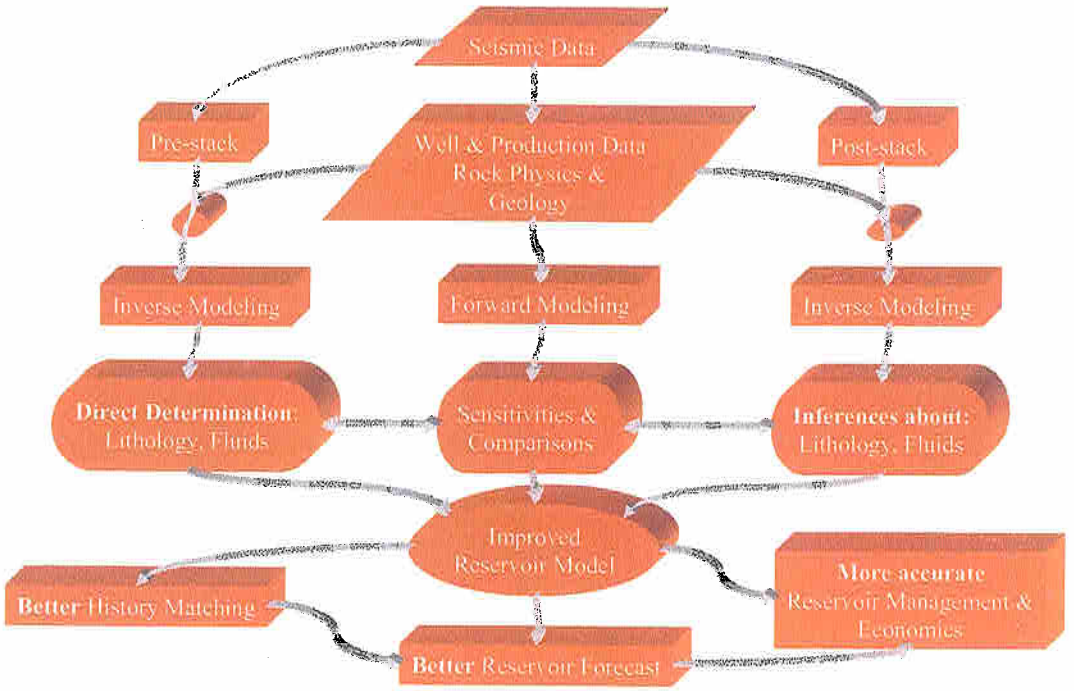

Figure B-2.1 Organization flow chart for integrated reservoir characterization studies.

Likewise, wireline logs and core data are routinely used to derive a first estimate of petrophysical variables in the vicinity of existing wells. Such estimates are then extrapolated away from existing wells via geostatistical techniques and upscaling procedures that yield a cellular reservoir model amenable to numerical simulation of multiphase fluid flow. The latter provide the input required for the economical assessment of a hydrocarbon field.

3. DESCRIPTION OF THE GEOLOGIC MODEL

The geologic model constructed for our study is shown in **Figure B-3.1**. A dominant background medium consists of a shale layer exhibiting a normal trend of mechanical compaction. There are two sand bodies embedded in the shale background representing sand lenses of fluvial architecture. The upper sand unit is saturated with water, whereas the lower sand unit is saturated with oil. Both geometry and dimensions of the sands were designed to quantify the spatial resolution of seismic data under complex geometrical conditions and tuning. Moreover, the dimensions of the model lend themselves to the simulation of angle stacks of up to 45 degrees.

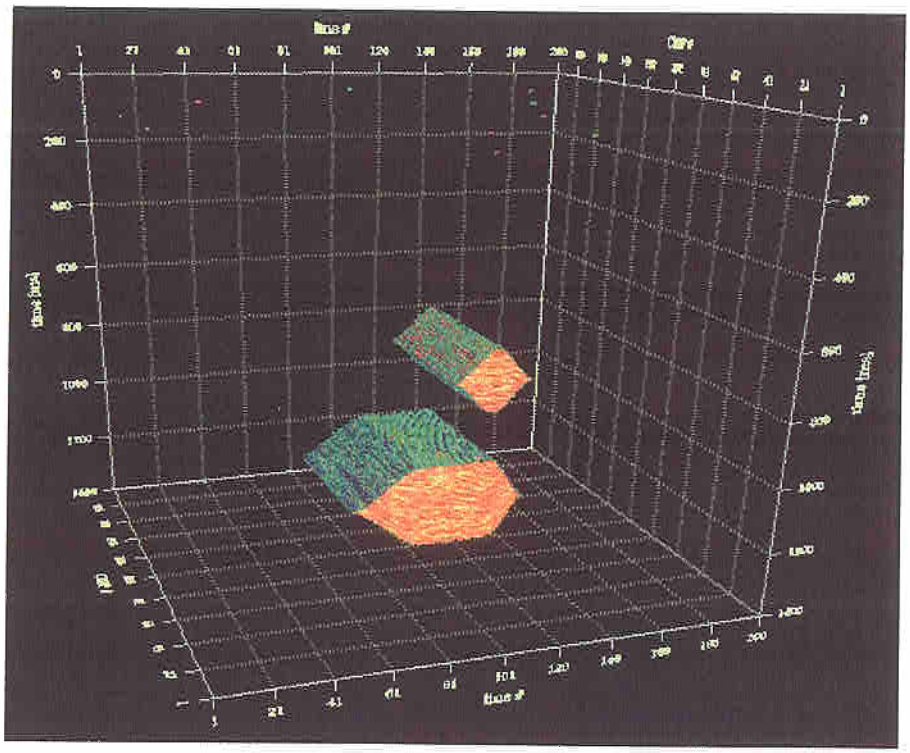

Figure B-3.1. Graphical description of the 3D synthetic geological model used for the numerical simulations of seismic and multi-phase fluid flow data described in this report.

4. ROCK PHYSICS MODEL

There are many relationships that link the elastic properties of rocks with their pore space, pore fluid, pressure, and composition. Many of these relationships are based on empirical correlations and are often applied to specific areas in the world where their validity has been confirmed by a number of experimental data (Hamilton, 1979, Castagna

et al., 1985). Others are based on wave theory and hence are subject to different kinds of assumptions (Gassmann, 1951, Biot, 1956). There is no single rock physics model that embodies a complete formulation. All of the know models have their own advantages and disadvantages. In the present study, we have explored the use of both empirical and theoretical approaches. Different rock physics models were considered to generate the main elastic properties, i.e. compressional velocity (V_p) and shear velocity (V_s). The use of additional relationships was also necessary in order to link the elastic parameters (i.e. bulk modulus) with petrophysical properties such as porosity, for instance.

4.1 Wave Equation.

For a homogenous and isotropic medium the general equation of motion may be written as:

$$\rho\frac{\partial^2 u}{\partial t^2} = (\lambda + 2\mu)(\nabla(\nabla \cdot u)) - \mu(\nabla \times \nabla \times u), \tag{4.1}$$

where u is the displacement. This equation implies that Newton's second law is defined in term of stress and displacement and that the stress and strain are proportional, i.e. that Hooke's law remains valid (for additional details on the wave equation see Elmore and Heald, 1969).

4.1.1 P-wave Propagation.

Taking the divergence of the equation of motion one has

$$\rho\frac{\partial^2(\nabla \cdot u)}{\partial t^2} = (\lambda + 2\mu)(\nabla \cdot \nabla(\nabla \cdot u)). \tag{4.2a}$$

If we now define the divergence of the vector displacement (u) as $\theta = \nabla \cdot u$ it follows that

$$\nabla^2\theta = \left(\frac{\rho}{\lambda + 2\mu}\right)\left(\frac{\partial^2\theta}{\partial t^2}\right), \tag{4.2b}$$

$$\nabla^2\theta = \left(\frac{1}{V_p^2}\right)\left(\frac{\partial^2\theta}{\partial t^2}\right), \tag{4.2c}$$

and

$$V_p^2 = \frac{\lambda + 2\mu}{\rho}, \tag{4.2d}$$

where,

λ is Lame's constant,

ρ is density,

μ is the shear (rigidity) modulus, and

V_p is compressional velocity.

4.1.2 S-wave Propagation.

Taking the curl of the equation of motion one obtains

$$\rho \frac{\partial^2 (\nabla \times u)}{\partial t^2} = \mu \left(\nabla^2 (\nabla \times u) \right). \tag{4.3a}$$

If we define the curl of the vector displacement as $\chi = \nabla \times u$ one obtains

$$\nabla^2 \chi = \left(\frac{\rho}{\mu} \right) \left(\frac{\partial^2 \chi}{\partial t^2} \right), \tag{4.3b}$$

or

$$\nabla^2 \chi = \left(\frac{1}{V_s^2} \right) \left(\frac{\partial^2 \chi}{\partial t^2} \right), \tag{4.3c}$$

with

$$V_s^2 = \frac{\mu}{\rho}, \tag{4.3d}$$

where V_s is shear velocity.

4.1.3 Additional Equations.

Some of the relationships among the elastic constants used are the bulk modulus, Poisson's ratio and Young's modulus. The bulk modulus, *k*, is given by

$$k = \lambda + \frac{2}{3} \mu . \tag{4.4}$$

On the other hand, Poisson's ratio, τ, can be written as

$$\tau = \frac{3k - 2\mu}{2(3k + \mu)} , \tag{4.5}$$

and the Young's modulus, E, as

$$E = \frac{9k\mu}{3k + \mu} \tag{4.6}$$

(for additional details on the relationships among the various elastic constant see, for instance, Sheriff, 1984).

4.2 Empirical Models.

Most of these models are based on experimental data and provide a direct calculation of V_p and/or V_s once other rock parameters are known. The literature has ample references for a sizable number of such experimental models. In this report we adopt the relationships introduced by Hamilton (1979) and Castagna et al. (1985).

4.2.1 Hamilton's (1979) Model.

The main objective of Hamilton's work was to establish a generalized relationship between V_p, V_s, V_p/V_s, and Poisson's ratio as a function of depth and for different classes of terrigenous sediments and sands. The main results of his work are relationships between among the elastic variables as a function of depth for each one of the major rock types. Equations 4.7, 4.8 and 4.9, for instance, describe the compressional and shear velocities of terrigenous sediments (i.e. silt-clays, turbidites, shales). These equations were calculated from rock data collected from different parts of the world:

$$V_p = 1.511 + 1.304D - 0.741D^2 + 0.257D^3, \tag{4.7}$$

where, V_p is given in km/s and D is given in km,

$$V_s = \begin{cases} 116 + 4.65D & 0 < D < 36 \\ 237 + 1.28D & 36 < D < 120 \\ 322 + 0.58D & 120 < D < 150 \end{cases}, \tag{4.8}$$

where, V_s is given in m/s and D is given in m, and

$$V_s = \begin{cases} 3.884V_p - 5.757 & 1.512 < V_p < 1.555 \\ 1.137V_p - 1.485 & 1.555 < V_p < 1.650 \\ 0.991 - 1.136V_p + 0.47V_p^2 & 1.650 < V_p < 2.150 \\ 0.78V_p - 0.962 & V_p > 2.150 \end{cases}, \tag{4.9}$$

where, V_p and V_s are given in km/s.

Equations 4.10 and 4.11 describe the compressional and shear velocity functions applicable to sands. Moreover, the functional relationships with depth is given by

$$V_p = 1806D^{0.015}, \tag{4.10}$$

and

$$V_s = 128D^{0.28}, \tag{4.11}$$

where, V_p and V_s are given in m/s and D is given in m.

4.2.2 Castagna et al.'s (1985) model.

Castagna et al. report relationships between compressional and shear wave velocities applicable to clastic silicate rocks. Measurements performed on a variety of water-saturated mudrocks suggest that Vp and Vs are controlled mainly by mineralogy. Making use of in-situ sonic and seismic data, the authors find the following relationship between Vp and Vs:

$$V_p = 1.16V_s + 1.36, \tag{4.12}$$

where velocities are given in km/s.

For sandstones, conventional log analysis was carried out on rocks sampled from the Frio Formation, in order to determine porosity (ϕ) and clay content (V_{cl}) from gamma ray, neutron and density logs. The resulting relationships for this formation are as follows:

$$V_p = 5.81 - 9.42\phi - 2.21V_{cl}, \tag{4.13}$$

and

$$V_s = 3.89 - 7.07\phi - 2.04V_{cl}, \tag{4.14}$$

where velocities are given in km/s, and ϕ and V_{cl} are given as dimensionless fractions. The correlation coefficient reported was 0.96 for both expressions. These results are similar to those reported by Tosaya (1982). It is possible to determine the values of V_p and V_s from a zero porosity clay (V_{cl} =1) and clean sand (V_{cl}=0) at a given porosity. It is also possible to establish V_p/V_s relations manipulating equations 4.13 and 4.14. These relationships show that as porosity and clay volume increase, the V_p/V_s also increases.

4.3 Theoretical Models.

Different theories have been put forth to describe the mechanical behavior of isotropic and homogenous rocks. In general terms, these theories they fall in two categories: the first category considers pore geometry while the second one is based on global properties. The models considered in this report fall into the second category since they provide more practical results (Castagna and Backus, 1993).

4.3.1 Biot-Gassmann

Gassmann's theory rests on the assumption that relative motion between the fluid and the skeleton has no influence on seismic wave propagation through fluid saturated rocks (Gassmann, 1951). This assumption is valid at low frequencies. The relative motion would cause loss in energy due to the viscosity of the fluid. Gassmann's theory does not provide a way to evaluate the effect of attenuation (White, 1983). However, Biot's theory is valid for a wider frequency range (Biot, 1956). Geertsman (1961) also developed equations valid for a wide frequency range based on the work of Biot. Equations 4.15 and 4.16 below summarize Geerstman's results:

$$V_p^2 = \left\{ \left(k_b + \frac{4}{3}\mu \right) + \frac{\frac{\phi\rho_b}{\kappa\rho_f} + \left(1 - \frac{k_b}{k_s}\right)\left(1 - \frac{k_b}{k_s} - \frac{2\phi}{\kappa}\right)}{\left(1 - \phi - \frac{k_b}{k_s}\right)\left(\frac{1}{k_s}\right) + \frac{\phi}{k_f}} \right\} \left\{ \frac{1}{\left(\rho_b - \frac{\phi\rho_f}{\kappa}\right)} \right\}, \qquad (4.15)$$

and

$$V_s^2 = \left\{ \frac{\mu}{\left(\rho_b - \frac{\phi\rho_f}{\kappa}\right)} \right\}, \qquad (4.16)$$

where the subscripts b, s, and f stand for bulk, solid (matrix), and fluid, respectively. Variable κ designates the mass coupling factor and varies from 1 (no fluid-solid coupling) to infinity (perfect coupling). For the case of perfect coupling, the above equations reduce to those of the zero-frequency (DC) limit, whereupon the velocities become frequency independent.

4.3.2 Duffy-Mindlin's (1957) Model.

Duffy and Mindlin (1957) derived elastic constants assuming a face-centered cubic array of identical spheres. It is interesting to remark how close this model reproduces a wide variety of velocities measured on rock samples (White, 1983). The main results of the Duffy-Mindlin model are given by

$$V_p^2 = \frac{\left\{ C_{11} + \frac{\left(1 - \frac{C_{11}+2C_{12}}{3k_s}\right)^2}{\frac{\phi}{k_f} + \frac{1-\phi}{k_s} - \frac{C_{11}+2C_{12}}{3k_s^2}} \right\}}{\rho_b}, \tag{4.17}$$

and

$$V_s^2 = \frac{C_{11}+C_{12}}{2\rho_b}, \tag{4.18}$$

where the subscripted C variables are given by the expressions

$$C_{11} = \frac{4-3\tau}{2-\tau}\left\{\frac{3E^2P_e}{8\left(1-\tau^2\right)^2}\right\}^{\frac{1}{3}}, \tag{4.19}$$

and

$$C_{12} = \frac{\tau}{2(2-\tau)}\left\{\frac{3E^2P_e}{8\left(1-\tau^2\right)^2}\right\}^{\frac{1}{3}}. \tag{4.20}$$

Equations 4.21, 4.22, and 4.23 below summarize the basic definitions of the mechanical parameters used in the Duffy-Mindlin model, namely,

$$P_e = P_{overburden} - P_{pore}, \tag{4.21}$$

$$\tau = \frac{3k_b - 2\mu_b}{2(3k_b + \mu_b)}, \tag{4.22}$$

and

$$E = \frac{9k_b\mu_b}{(3k_b + \mu_b)}, \tag{4.23}$$

where P is pressure.

4.4 Elastic Relationships.

Usage of experimental mechanical models requires information that is not normally available. The relationships found by Hamilton require knowledge of both depth and lithology to calculate velocities. Castagna's relationships provide velocity values based on porosity and volume of clay; lithology information is needed for the case of a pure rock system. On the other hand, expressions associated with the theoretical models described above require knowledge of the bulk moduli of the rock, fluid, and matrix, of the rock's bulk rigidity modulus, and of the effective pressure, density, and porosity. A simple, yet practical way to define these material properties is to make use of a combination of the values associated with pure components. Table B-4.1 describes common values obtained from the literature for the elastic parameters of various pure components. Our interest in providing specific values for these components obeys to a subsequent need to simulate numerically multi-phase flow and seismic data.

Table B-4.1. Elastic parameters associated with pure rock components.

Pure Component	Bulk Modulus (Mpa)	Shear Modulus (Mpa)	Density (g/cc)
Sand	36e9	32e9	2.65
Shale	22e9	6.8e9	2.85
Water	2.3e9	-	1.00
Oil	1.6e9	-	0.87

4.4.1 Bulk Density.

As described by equations 4.24a and 4.24b, the bulk density (ρ_b) is a simple linear weighted average with weights given by the volume fraction of each component, i.e.,

$$\rho_b = \sum_{i=1}^{N} v_i \rho_i \ , \qquad (4.24a)$$

where v_i is the volume fraction of the i-th component. In the case of a system with two lithologies (i.e. sand and shale) and two fluids (i.e. oil and water) the last equation becomes

$$\rho_b = ((1-\phi)V_{cl})\rho_{sh} + ((1-\phi)(1-V_{cl}))\rho_{ss} + (\phi S_w)\rho_w + (\phi(1-S_w))\rho_o \ . \quad (4.24b)$$

We remark that the expressions between parentheses in each additive term above correspond to the volume fraction of each existing component (v_i).

4.4.2 Fluid Bulk Modulus.

The fluid modulus was calculated as the harmonic average of each one of the pure components weighted by their respective volume fraction, i.e.,

$$\frac{1}{k_f} = \sum_{i=1}^{N} \frac{S_i}{(k_f)_i} \quad , \quad (4.25)$$

where S_i is the saturation of the i-th fluid and N is the total number of fluid components.

4.4.3 Dry Bulk Modulus

The theoretical formulation for determining elastic parameters of rocks from their petrophysical properties requires knowledge of the rock's dry bulk modulus. Geertsman and Smith (1961) defined an empirical relation among the bulk modulus, matrix modulus, and porosity, given by

$$\frac{k_b}{k_s} = \frac{1}{(1+50\phi)}. \quad (4.26)$$

Hamilton (1971) established similar empirical relationships in terms of the rock's matrix bulk modulus and its porosity. A simple formula applicable to clastic sediments is written as

$$\frac{k_b}{k_s} = 10^{-4.25\phi} \quad . \quad (4.27)$$

4.4.4 Shear Bulk Modulus.

The main assumption made when estimating elastic parameters of rocks is that the interstitial fluid does not interact with the matrix. This assumption causes the shear modulus of the fluid-saturated rock to be equivalent to that of the dry rock, i.e.

$$\mu_b = \mu_s . \tag{4.28}$$

4.5 Comparison Among the Various Fluid-Substitution Models.

The experimental and theoretical fluid substitution models described above were tested over our synthetic 3D geologic model. A comparison of the ensuing results is shown in **Figure B-4.1**. All the necessary input data are known beforehand (i.e. porosity, saturation, effective pressure, etc). The experimental formulation of Hamilton's requires knowledge of both depth and lithology to calculate the corresponding P- and S-wave velocities. This approach gives a consistent depth trend for the velocities, but remains independent of fluid content, porosity, and effective pressure. On the other hand, Castagna's model requires as input the porosity, and the volume of clay (or else the lithology) in the case of a pure component system. In this case, velocities are computed taking into account the porosity although ignoring both fluid content and pressure. Velocities can change laterally, however, if two points at different depths exhibit the same porosity. This means that the normal velocity trends are not always satisfied by Castagna's model (Varela et al., 2001). **Figure B-4.1** is a graphical summary of the elastic parameters as a function of depth calculated with different rock physics/fluid substitution models across our synthetic reservoir model. In particular, the curve labeled "1" in **Figure B-4.1** identifies the elastic parameters calculated via Castagna's model.

The theoretical rock physics models were also evaluated using the two empirical relations of the dry bulk modulus. In **Figure B-4.1**, results from equation 4.26 are identified with the letter a, and those following from equation 4.27 are identified with the letter b. Biot-Gassmann-Geertsman's theoretical model was tested for the limiting cases of κ equal to infinity and one. The corresponding results are shown in **Figure B-4.1** with the curves identified with the numbers "2" and "3," respectively (Varela, 2002). Even though the latter model does take into account porosity changes, fluid content, etc., the calculated depth behavior of the velocities is not always internally consistent. Duffy and

Mindlin' model, on the other hand, does include effective pressure in the calculations and therefore is able to recover a consistent depth trend for the velocities. Results from this model, identified with the number "4" in **Figure B-4.1**, provide a consistent behavior with respect to depth including the effect of mechanical compaction (Varela et al, 2001). The two approaches used for calculating the bulk modules yield similarly consistent results. Given that Duffy and Mindlin's rock physics model provided the most accurate behavioral results, henceforth we make use of this model for subsequent fluid calculations, including those described by equation 4.26 in connection with the bulk modulus.

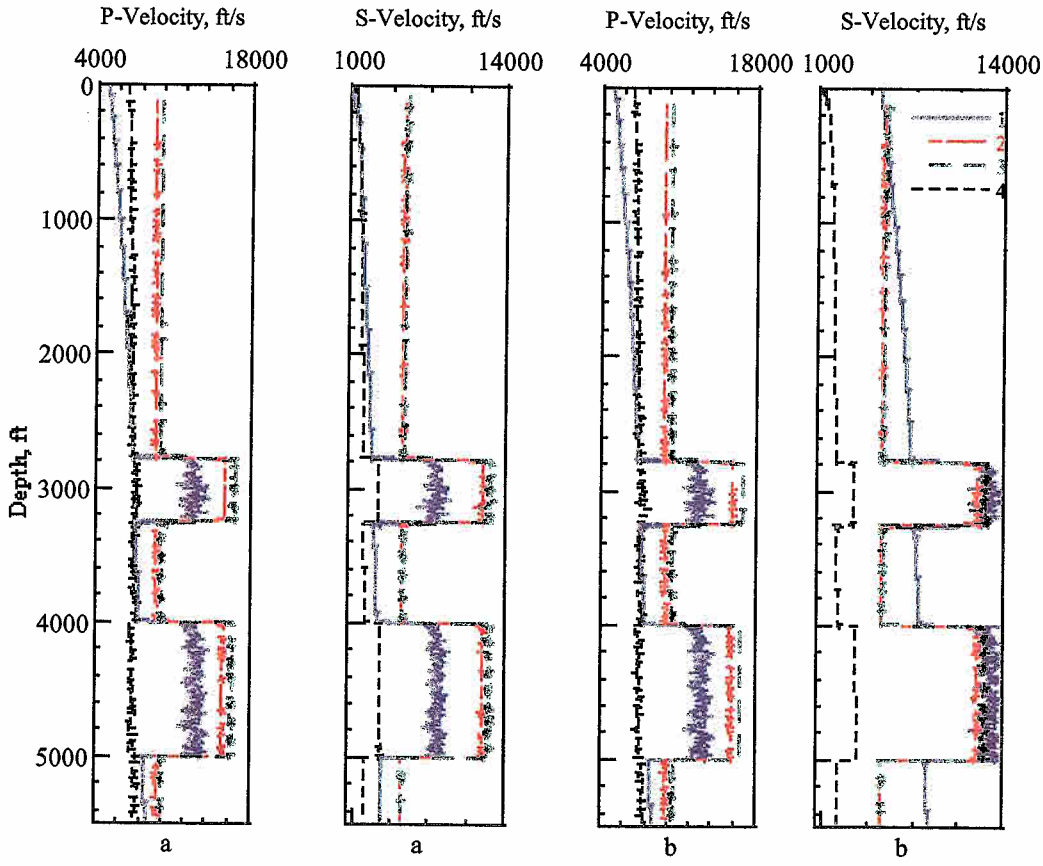

Figure B-4.1. Graphical comparison of the P- and S-wave velocities as a function of depth calculated using various rock physics/fluid substitution models. Calculations were performed using the synthetic reservoir model described in **Figure B-3.1**. The vertical profiles shown above intersect both the background shale layer and the lower, oil saturated sand unit.

5. RESERVOIR PARAMETERS

Petrophysical properties within the synthetic reservoir model were simulated using lithology-dependent probability density functions and semi-variograms. There were only two lithologies considered in the simulations, namely, sand and shale. Also, the simulations were made consistent with the global trend of mechanical compaction as a function of depth. **Figures B-5.1** and **B-5.2** shows plots with respect to depth of various elastic parameters simulated across the shale background described in **Figure B-3.1**.

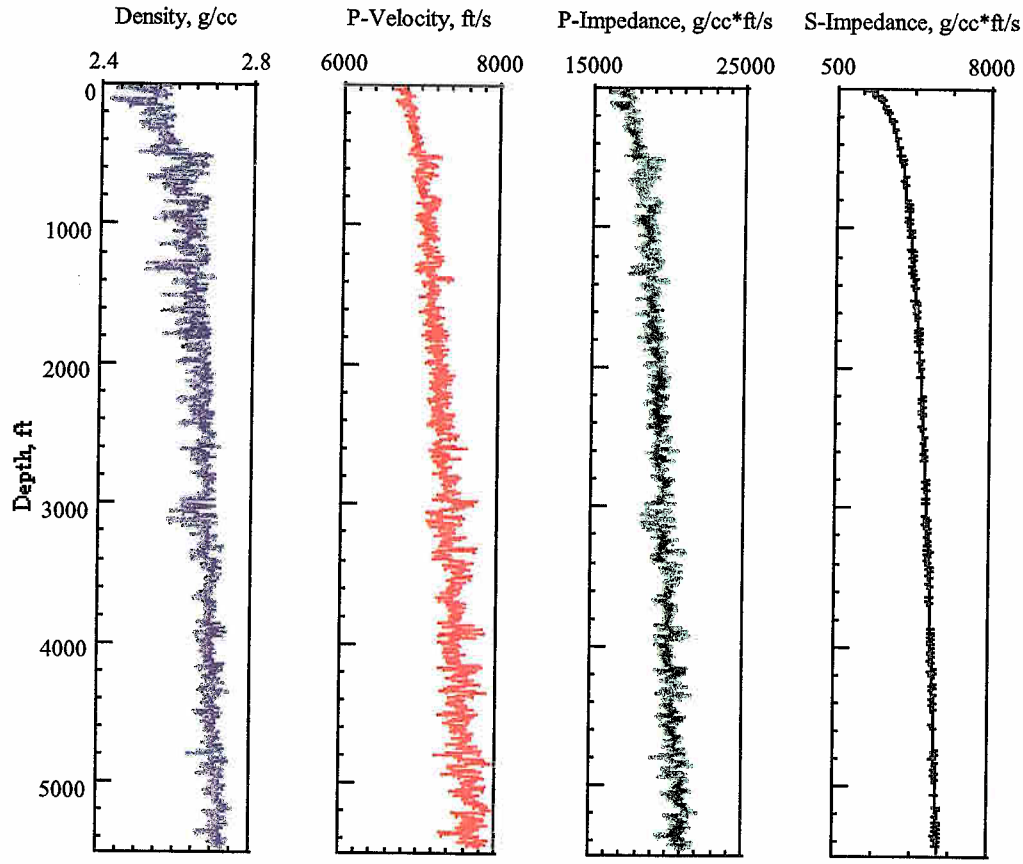

Figure B-5.1 Plot of the depth variations of the various elastic parameters calculated across the shale background of the 3D reservoir model shown in **Figure B-4.1**.

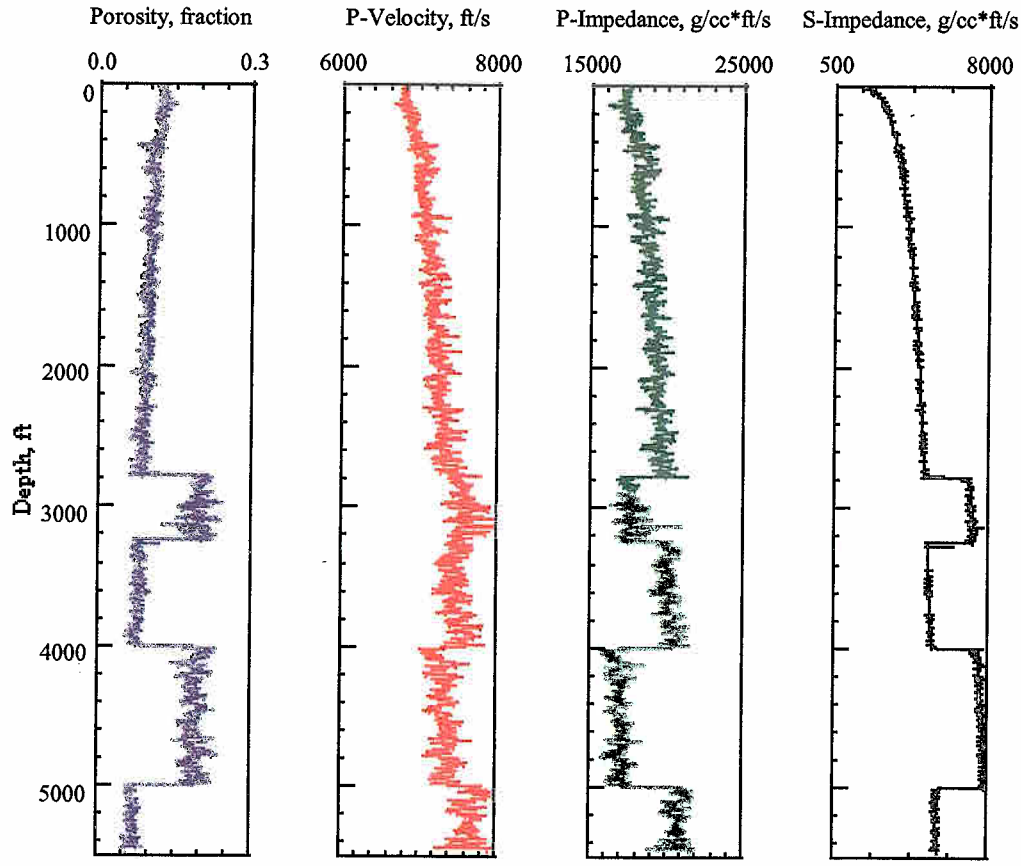

Figure B-5.2. Plot of the depth variations of the various elastic parameters calculated across the oil-filled reservoir sand (the lower-most sand) of the 3D reservoir model shown in **Figure B-4.1**.

5.1 Porosity

A porosity distribution within the geological model of **Figure B-4.1** was constructed via geostatistical techniques. This was accomplished using as interpolation/extrapolation geometrical framework a horizontal layering within the shale background, and a fluvial layering within the two existing sands. Stochastic realizations of porosity were obtained with a sequential collocated Gaussian co-simulation procedure. The global porosity field was assumed to be second-order stationary, normally distributed, and exhibiting a prescribed semi-variogram. The second simulated variable was the compaction trend for porosity. This compaction trend originates from vertical overburden stress due to geostatic load, and is calculated using the deterministic equations of Bourgoyne, et al. (1991). **Figure B-5.3** shows the 3D porosity model simulated across the oil-saturated sand of the model in **Figure B-4.1**.

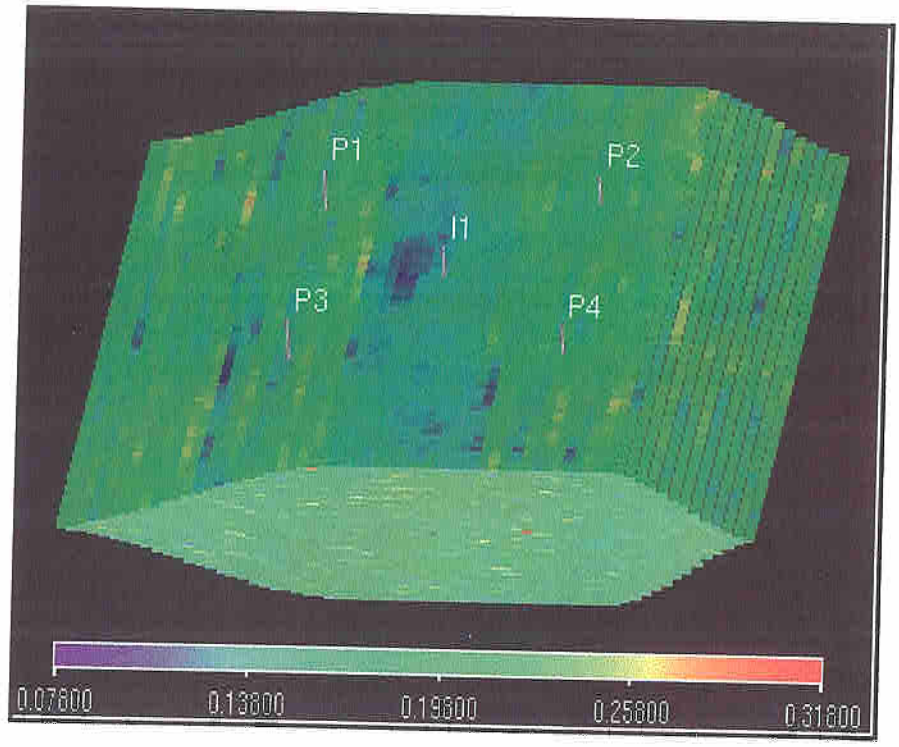

Figure B-5.3. Three-dimensional rendering of the porosity distribution simulated within the oil-saturated sand of **Figure B-4.1**.

In order to explain how the simulation of porosity was performed, first let us suppose that we know property X in N different locations (i.e. locations along wells) and that we want to estimate that property in an unknown location, k. A way to perform this simulation is by making use of weighted linear average of the known values of X, i.e.,

$$\hat{X}_k = \sum_{i=1}^{N} \lambda_i X_i \,, \tag{5.1}$$

where the λ coefficients are the only unknowns. By defining the simulation error as the difference between the estimation and the true value one obtains

$$\varepsilon = X_k - \hat{X}_k = X_k - \sum_{i=1}^{N} \lambda_i X_i \tag{5.2}$$

One way to determine the λ coefficients is to minimize the variance between the interpolated and true values of X. This is equivalent to minimizing the expected value, (E{.}), of the square of the prediction error, i.e.

$$E\{\varepsilon^2\} = E\left\{\left(X_k - \sum_{i=1}^{N} \lambda_i X_i\right)^2\right\}. \tag{5.3}$$

The stationary points of the squared error above are determined by taking the partial derivatives of the mean square error with respect to each of the weights, λ's, and by setting them to zero, i.e.

$$0 = E\left\{2\left(X_k - \sum_{i=1}^{N} \lambda_i X_i\right)\left(\sum_{i=1}^{N} X_i \delta_r^i\right)\right\} \; for \; r = 1....N \tag{5.4}$$

where δ_r^i=1 if i=r and 0 otherwise. By defining $X_r = \sum_{i=1}^{N} X_i \delta_r^i$, we obtain

$$E\{X_k X_r\} = E\left\{\sum_{i=1}^{N} \lambda_i X_i X_r\right\} for \; r = 1....N. \tag{5.5}$$

Parenthetically, a general definition of covariance between two variables (U and V) can be written as

$$C(U,V) = E\{(U - E\{U\})\}E\{(V - E\{V\})\}. \tag{5.6}$$

By assuming zero mean processes in equation 5.6, one obtains

$$C(U,V) = E\{U\}E\{V\}. \tag{5.7}$$

In consequence, equation 5.5 can be rewritten as

$$\sum_{i=1}^{N} \lambda_i C_{XX}(i,r) = C_{XX}(k,r) \; for \; r = 1.....N. \tag{5.8}$$

The parameters λ's can be readily obtained by solving the linear system of equations 5.8. This in turn yields a value for the property X at a given location within the model. In our case, the covariance matrix is calculated from both the probability density function and the semi-variogram. The additional contribution due to compaction can be included in the calculation via the expression

$$X_k = \sum_{i=1}^{N} \lambda_i X_i + \sum_{j=1}^{M} \beta_j Y_j, \qquad (5.9)$$

where the variable Y designates the additive component of porosity due to compaction, and the weights β are to be determined by a minimization procedure similar to that described earlier in connection with the λ coefficients. Because the stochastic simulation of porosity is collocated in nature, there is no need to enforce a semi-variogram for the secondary variable (compaction component); only a measure of the correlation between the two variables is necessary.

5.2 Permeability

Absolute permeability is perhaps the single most important petrophysical variable that governs the physics of fluid flow. It is also one of the most difficult variables to assess because of its high spatial variability and wide range of values. Often, permeability bears a deterministic relationship with porosity and as such remains affected by grain size and shape, pore-size distribution, and grain packing, among other variables. Several relationships between permeability and porosity have been reported in the technical literature. As exemplified by **Figure B-5.4**, most of these relationships describe permeability as an exponential function of porosity.

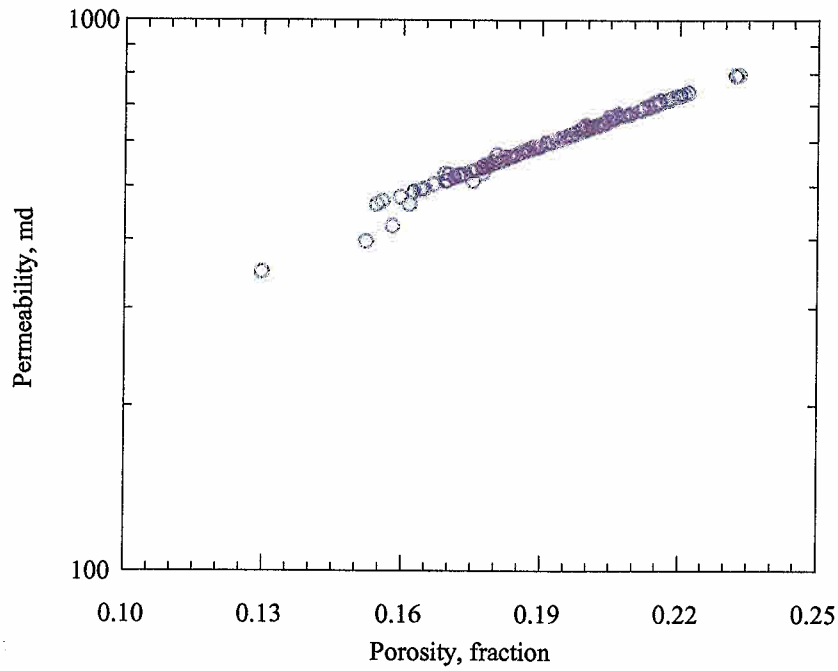

Figure B-5.4. Plot of the assumed relationship between absolute permeability and porosity.

5.3 Relative Permeability Curves

Relative permeabilities are necessary to evaluate the fluid-flow performance of multi-phase systems. The relative permeability of a porous and permeable rock is a function of the fluid's mobility, which at the same time is determined by the rock's wettability and capillarity. For the purpose of the fluid-flow simulations described in this report, we concentrate on a water-wet porous rock system governed by the set of relative permeability curves shown in **Figure B-5.5**.

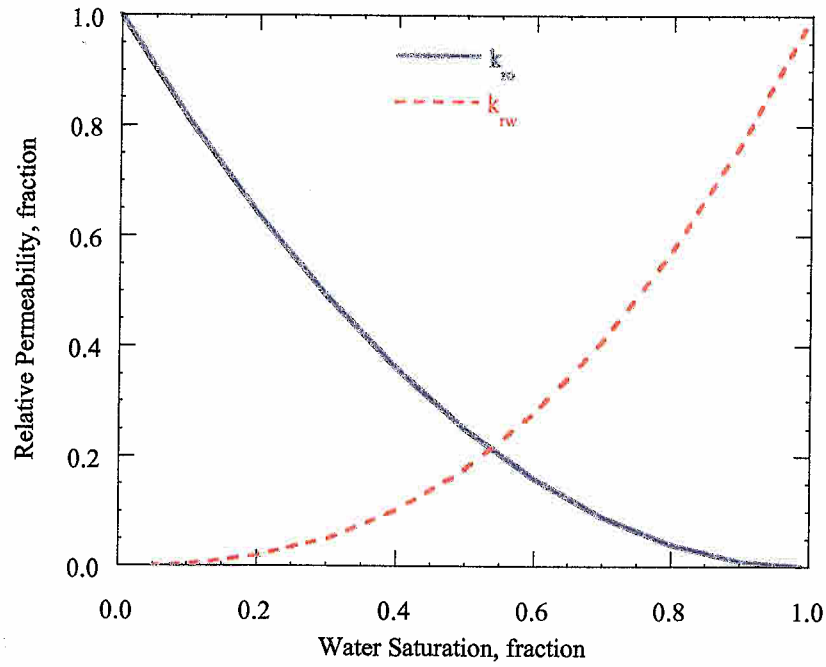

Figure B-5.5. Plot of the normalized water-oil relative permeability curves used in the fluid-flow simulations described in this report.

In this report, a deterministic power law is adopted to govern the dependency of relative permeability on water saturation. This power-law relationship is defined in the following manner. First define a reduced water saturation as

$$S_w^* = \frac{S_w - S_{wi}}{1 - S_{or} - S_{wi}}. \tag{5.10}$$

The relative permeability functions are then given by

$$k_{rw}\left(S_w^*\right) = k_{rw}^o S_w^{*n}, \tag{5.11}$$

and

$$k_{ro}\left(S_w^*\right) = k_{ro}^o (1 - S_w^*)^m, \tag{5.12}$$

where k_{rw}^{o} and k_{ro}^{o} are the end-point values of the water-oil relative permeabilities, and n and m are the water and oil saturation exponents, respectively (Lake, 1989). For the fluid-flow simulations described in this report, we calculated residual water saturations using their determinist dependency with porosity (Tiab and Donaldson, 1996), whereas the end points of the water-oil relative permeability curves were calculated using the empirical relationships developed by Hornarpour et al. (1982).

6. FLUID-FLOW MODEL AND SIMULATIONS

For our reservoir simulations, we assumed a multi-phase fluid-flow process governed by a five-spot water-flooding scheme (one water injection well and four equally-spaced hydrocarbon producing wells). Water flooding is a widely used enhanced-oil-recovery wherein water is injected to improve the production performance of the reservoir.

6.1 Mathematical Formulation.

Simulation of multi-phase fluid-flow phenomena in porous media requires of a mass equation, a transport equation, and a constituent equation. The mass equation for the *i*-th fluid phase (either water or oil in our case) is given by

$$\frac{\partial(\rho_i \phi S_i)}{\partial t} + \vec{\nabla} \cdot (\rho_i \vec{v}_i) = -q_{vi}, \tag{6.1}$$

where ρ is fluid density, v fluid velocity, ϕ porosity, and q_v is a source-sink term (the driving source term). On the other hand, the transport equation is Darcy's law, written as

$$\vec{v}_i = -\vec{\vec{k}} \cdot \frac{k_{ri}}{\mu_i} \left(\vec{\nabla} P_i - \gamma_i \vec{\nabla} z \right), \tag{6.2}$$

where $\vec{\vec{k}}$ is the absolute permeability tensor of the porous medium, k_r is the relative permeability, μ is the fluid viscosity, and γ is the specific gravity of the fluid. Finally, the constituent equation follows from the equation of state. We further assume that both fluid and rock compressibility are constant over the pressure range of interest; their corresponding expressions are given

$$c_{fl} = -\frac{1}{V}\frac{\partial V}{\partial P}\bigg|_T = \frac{1}{\rho}\frac{\partial \rho}{\partial P}\bigg|_T,$$

and

$$c_r = \frac{1}{\phi}\frac{\partial \phi}{\partial P}\bigg|_T.$$

(6.3)

In the above expressions, capillary pressures and fluid saturations are governed by

$$P_c(S_w) = P_o - P_w, \tag{6.4}$$

and

$$S_o + S_w = 1, \tag{6.5}$$

respectively.

6.2 Reservoir Simulation.

We made use of a commercial finite-difference code to simulate the multi-phase water-flooding process described above. A simulation grid was constructed within the oil-saturated sand (**Figures B-3.1** and **B-4.1**) using a total of 81x81x102 nodes in the x, y, and z, directions, respectively, of uniform dimensions equal to approximately ~23mx23mx3m. The same grid was used to simulate the corresponding seismic data and hence there was no need to perform upscaling when deriving a distribution of elastic parameters from petrophysical variables. As emphasized earlier, the end point of the relative permeabilities curves were scaled and so were well residual water saturations. Water injection was set to a constant pressure, whereas fluid production was controlled with reading of bottomhole pressure. The water-flooding production schedule was run for a period of eight years. As designed, the reservoir model provides all of the necessary petrophysical variables in space and time to calculate elastic parameters via Duffy and Mindlin's rock physics model.

6.3 Simulation Results.

Figure B-6.1 shows plots of (a) cumulative oil production, (b) cumulative injected water, and (c) cumulative produced water, simulated for our synthetic reservoir over a

period of 3,000 days (approximately 8 years). These plots show that oil production starts to deviate from a straight line as soon as the water breakthrough takes place. Similarly, **Figure B-6.2** shows plots of (a) oil recovery, (b) average water saturation, and (c) water cut, measured during the same period of time considered in **Figure B-6.1**.

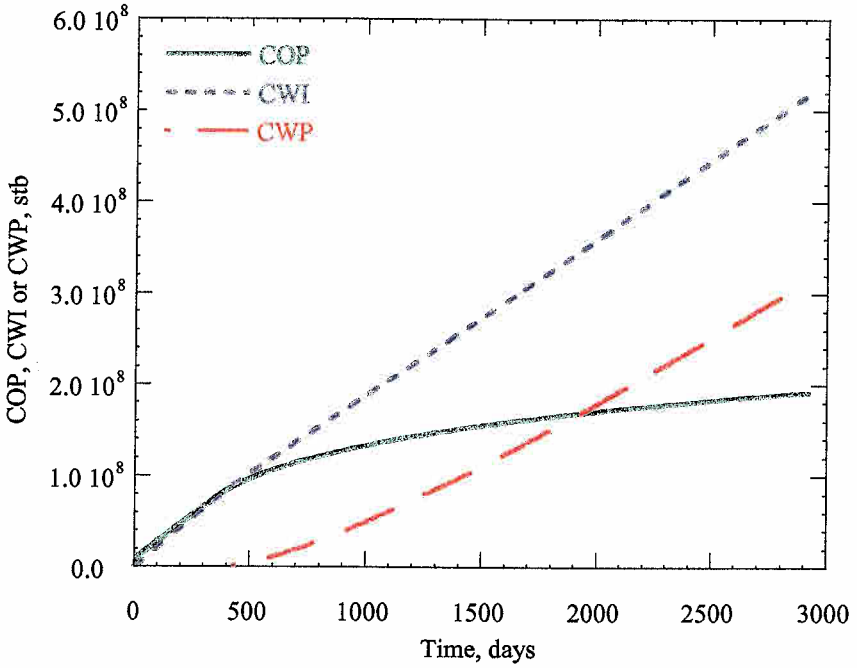

Figure B-6.1. Plot of the time evolution of the cumulative fluid production (oil and water) and injection (water).

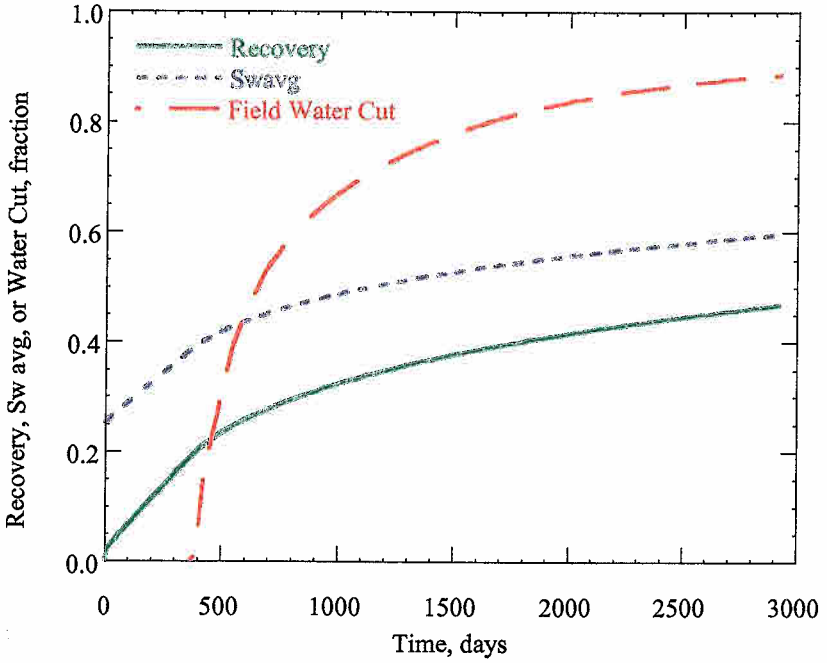

Figure B-6.2. Plots describing the time evolution of (a) water-flood recovery, (b) average water saturation, S_w, and (c) water cut.

For the purposes of this report, the most important outputs from the water-flood simulation described above are the spatial distributions of fluid saturation (i.e. water and oil) and pore pressure. Snapshots of these distributions were "captured" at the times t_0=0, t_1=4 and t_2=8 years after the onset of production. As shown below, the calculation of elastic parameters (bulk density, P-, and S-wave velocities) follows directly from the spatial distribution of porosity and from the computed distributions of fluid saturation and pore pressure.

6.4 Analysis of Elastic Parameters.

Histograms of petrophysical variables and elastic parameters were sampled from the reservoir simulations described above in order to explore and quantify any existing relationship between the two sets of variables. These histograms, shown in **Figure B-6.3**, were sampled along a hypothetical vertical well intersecting the oil-saturated sand shown in **Figure B-4.1** at three different times during reservoir production, namely, t_0=0, t_1=4, and t_2 = 8 years after the onset of production.

We remark that pressure changes between t_0 and t_1 are considerable, whereas those between t_1 and t_2 are negligible. In fact, pressure at time t_2 is greater than pressure at time t_1 as a consequence of the water injection process. Also, despite the fact that changes in water saturation are substantial, bulk density does not exhibit significant changes. Such an unfavorable situation occurs because of the small difference in oil and water density. Because of this, the observed changes in compressional- and shear-wave velocity are predominantly due to changes in pore pressure and water saturation.

Varela (2002) performed a detailed study of the sensitivity of Duffy and Mindlin's rock physics model to each petrophysical parameter. He used the values described in Table B-4.1 to calculate the corresponding changes in compressional- and shear-wave velocity due to changes in porosity, water saturation, and effective pressure. **Figure B-6.4** shows the relative changes between t_0 and t_1 in pore pressure and water saturations and the associated relative changes in compressional- and shear-wave velocity. This analysis showed that compressional velocity was predominantly affected by saturation and pressure changes whereas shear velocity was mainly affected by pressure changes.

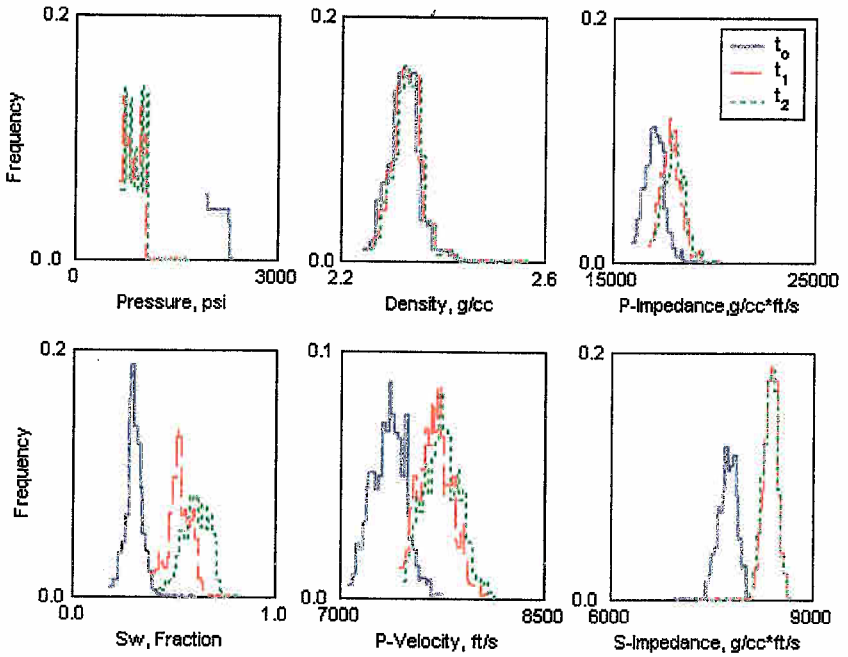

Figure B-6.3. Histograms of water saturation and pore pressure, and of their corresponding elastic parameters sampled along a hypothetical vertical well intersecting the oil-saturated sand shown in **Figure B-4.1**. Sets of histograms are shown for times $t_0 = 0$, t_1=4, and t_2= 8 years after the onset of production.

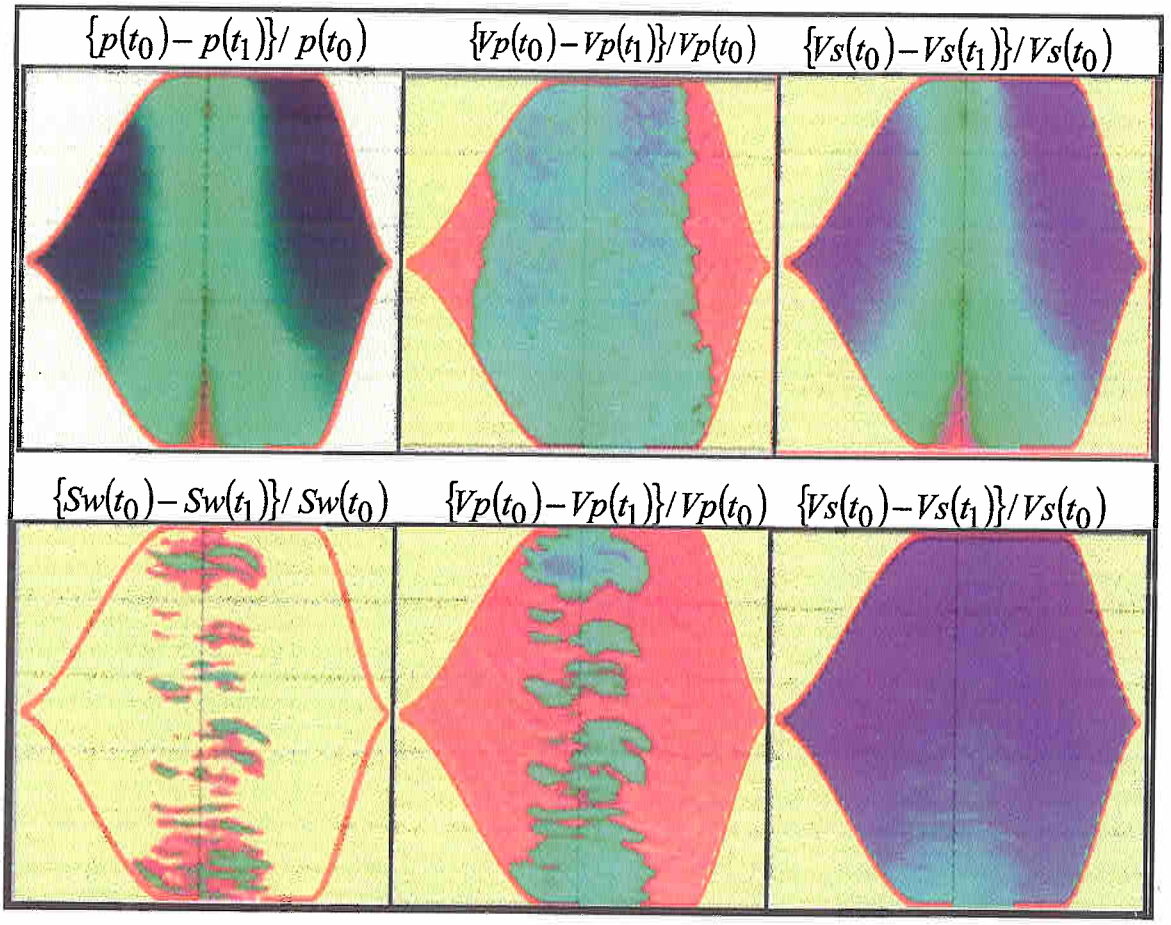

Figure B-6.4. Sensitivity of elastic parameters to time-domain variations of petrophysical properties. The panels above show relative differences with respect to time of (a) water saturation, (b) effective pore pressure, (c) P-wave velocity, and (d) S-wave velocity, corresponding to two time snapshots in the production life of the reservoir (t_1-t_0, where t_0 is 0 years and t_1 is 4 years after the onset of production.)

7. SEISMIC FORWARD MODELING

As emphasized earlier, 3D distributions of bulk density, and compressional- and shear-wave velocity were calculated using Duffy and Mindlin's rock physics model together with petrophysical data rendered by fluid-flow simulation. Such distributions of elastic parameters were subsequently used to simulate volumes of post- and pre-stack seismic data at the nominal times of t_0, t_1, and t_2 after the onset of production. Prior to performing the simulation of seismic data, the distributions of elastic parameters were transformed from depth into seismic time using the calculated distribution of P-wave

velocities. A sampling interval of 2 milliseconds (ms) was adopted for all the simulations of seismic data described in this report.

7.1 Simulation of Post-Stack Seismic Data.

We assumed local one-dimensional distributions of acoustic impedance to simulate post-stack seismic data across the distribution of elastic parameters. This was accomplished by way of a convolutional model implemented with a zero-phase Ricker wavelet centered at 35 Hz (**Figure B-7.1**) Three cubes of post-stack seismic data were produce corresponding to nominal values of reservoir production time of t_0=0, t_1=4, and t_2=8 years.

Acoustic impedance is a material property defined as the product of bulk density times compressional-wave velocity, i.e.

$$AI = \rho V_p . \tag{7.1}$$

In turn, reflection coefficients respond to interfaces between adjacent media that exhibit differences in their acoustic impedances. The following equation is used to calculate reflection coefficients from values of acoustic impedance:

$$R = \frac{AI_2 - AI_1}{AI_2 + AI_1} . \tag{7.2}$$

Post-stack seismic data are computed as the output of a time-domain convolution process between the sequence of reflection coefficients and an input wavelet, W. This convolutional model is formally written as

$$S(t) = R(t) * W(t) , \tag{7.3}$$

where *S(t)* is the simulated seismogram.

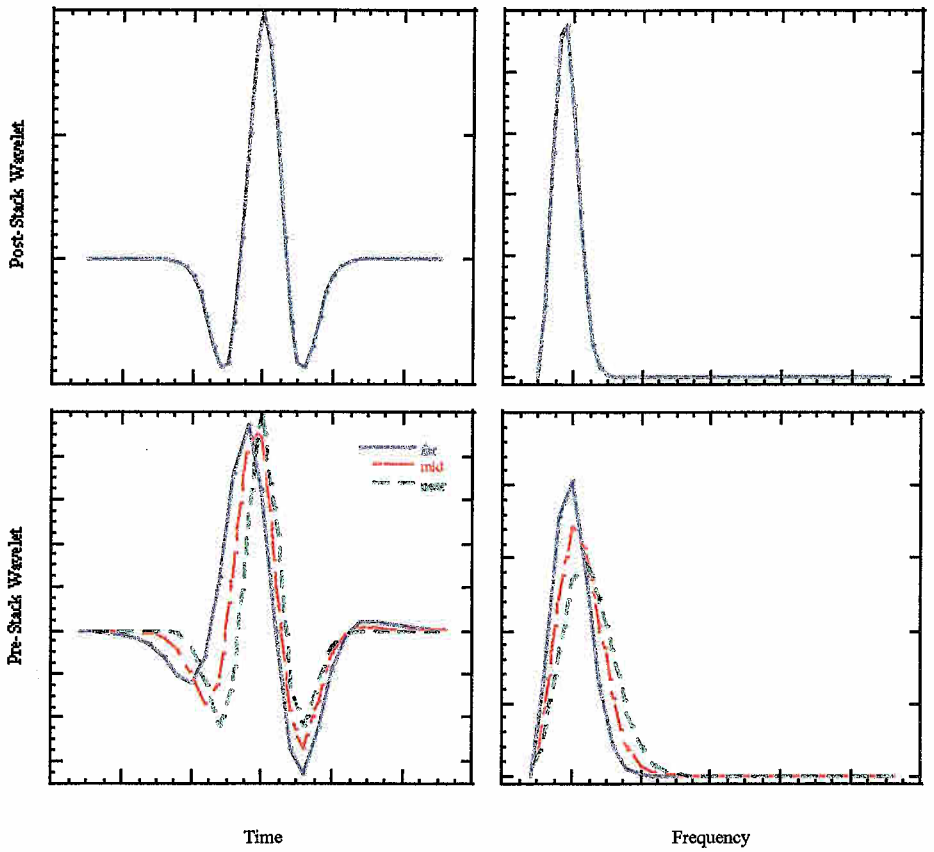

Figure B-7.1. Synthetic wavelets used for the numerical simulation of post- and pre-stack seismic data. The upper panels show the time- and frequency-domain counterparts of the zero-phase Ricker wavelet used in this report to simulate post-stack seismic data. The lower panels show the time- and frequency-domain counterparts of three wavelets used to simulate the pre-stack seismic data at near, mid, and far offsets, respectively.

7.2 Simulation of Pre-Stack Seismic Data.

Knott (1899) and Zoeppritz (1919) derived expressions for the reflection and transmission coefficients of planar interfaces as a function of the angle of incidence of seismic plane waves. These expressions were obtained by enforcing the continuity of displacement and stress at the reflecting interface (Aki and Richards, 1980). The exact equations of the P-P reflection (R_{pp}) and Transmission (T_{pp}) coefficients can be written as a function of the ray parameter (p) in the following manner

$$R_{pp} = \frac{E + Fp^2 + Gp^4 - Dp^6}{A + Bp^2 + Cp^4 + Dp^6}, \tag{7.4}$$

and

$$T_{pp} = \frac{H + Ip^2}{A + Bp^2 + Cp^4 + Dp^6}, \tag{7.5}$$

where $p = \frac{\sin\theta}{V_p}$ and the remaining coefficients in capital letters (A, B, C, etc) are functions of density and of the compressional and shear velocities. In other words, these coefficients are only indirectly related to the ray parameter. As a consequence, Knott-Zoeppritz equations are highly nonlinear with respect to the velocities and densities.

We simulated pre-stack seismic data along three angle intervals and for the three nominal values of reservoir production time of t_0=0, t_1=4, and t_2=8 years. The angle intervals considered in our simulations were near (0-15°), mid (15-30°), and far (30-45°) offset, respectively. Each angle interval is equivalent to what is normally referred to as an angle pseudo-stack in the jargon of applied seismology. Our three angle pseudo-stacks were generated using the Knott-Zoeppritz equation and the three synthetic wavelets shown in **Figure B-7.1**.

7.3 Simulation of Seismic Acquisition Noise.

The simulated post- and pre-stack seismic data were contaminated with additive noise in an effort to quantify the effects of realistic levels of measurement noise. Additive noise was derived from the output of a zero-mean, uncorrelated Gaussian random number generator. The standard deviation of the random number generator was chosen such that the signal-to-noise energy ratio was approximately equal to 1:10.

7.4 Seismic Results.

Figure B-7.2 is a cross-section of the simulated post-stack seismic data taken along the center of the model shown in **Figure B-3.1** at the beginning of the production schedule (time= t_0= 0 years). The vertical scale of the cross-section is double travel time and spans a total of 1,500ms.

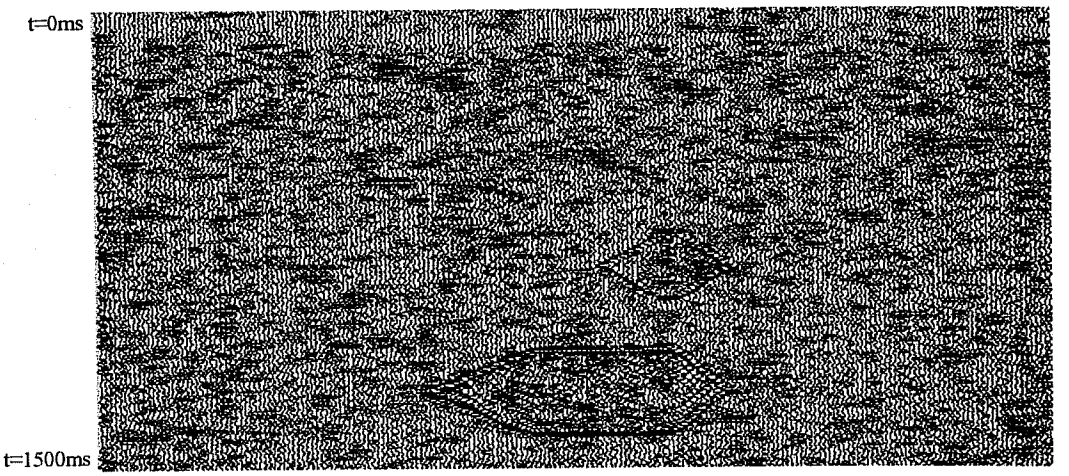

Figure B-7.2. Cross-section of the post-stack seismic data simulated at reservoir production time $=t_0=0$ years. Ten percent additive Gaussian noise was added to the simulated seismic data.

Figure B-7.3 shows the corresponding cross-sections of pre-stack seismic data simulated along the center of the model of **Figure B-3.1** at reservoir production time = $t_0= 0$ years. The three seismic cross-sections shown in **Figure B-7.3** correspond to near (top panel), mid (central panel), and far (lower panel) offsets, respectively with their vertical scales given double travel time. Similar cross-sections were simulated at reservoir production times equal to 4 and 8 years after the onset of hydrocarbon production.

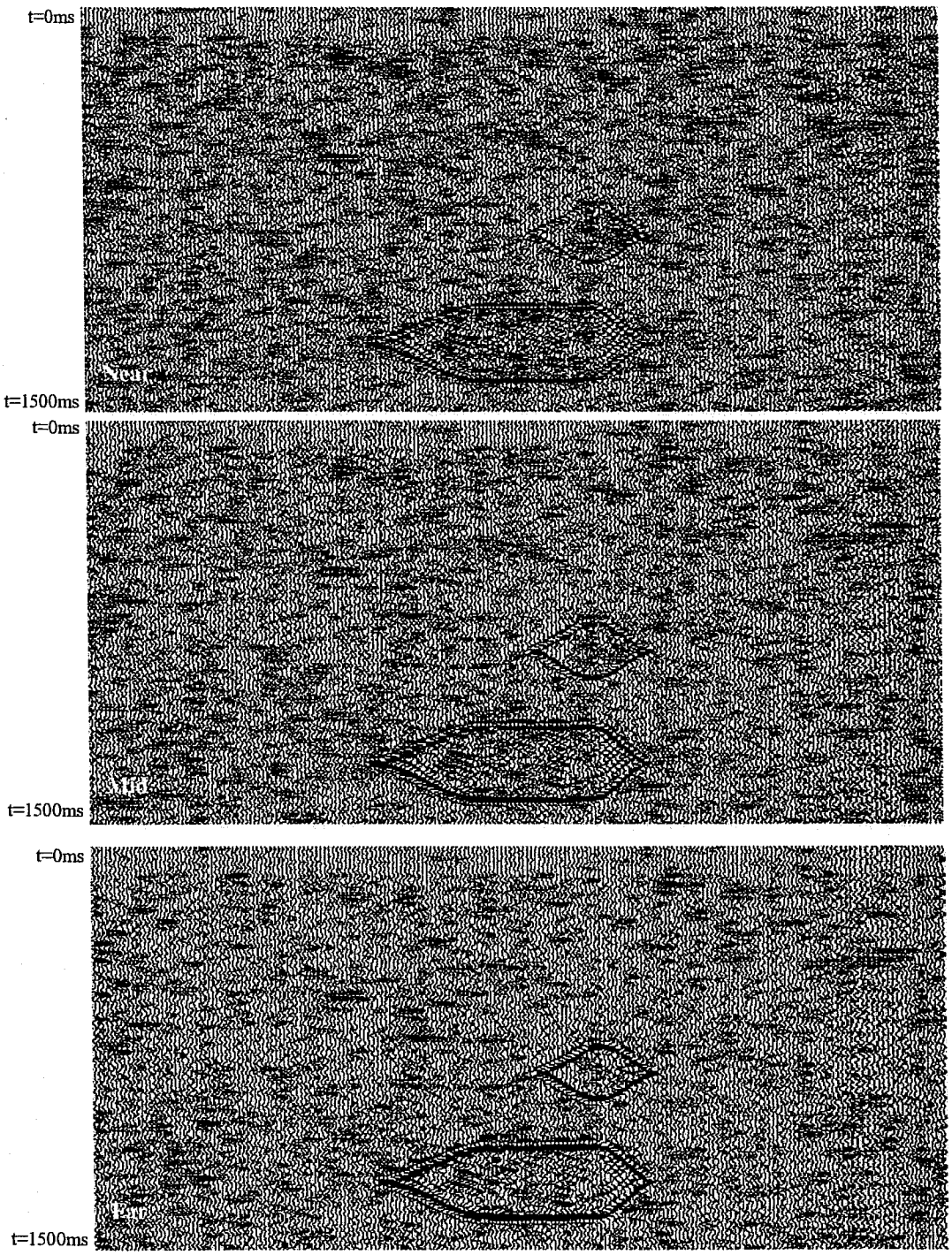

Figure B-7.3. Cross-sections of the pre-stack seismic data simulated at reservoir production time $=t_0=0$ years. Ten percent additive Gaussian noise was added to the simulated seismic data. The three panels show pre-stack seismic data simulated at near (top panel), mid (central panel), and far (lower panel) offsets, respectively.

8. SEISMIC INVERSE MODELING

Interpretation of 3D seismic data often relies on amplitudes analysis to identify anomalies that could be associated with petrophysical properties of hydrocarbon reservoirs. However, petrophysical interpretation directly from seismic amplitudes can be unreliable and inaccurate due to wavelet and tuning effects as well as deleterious measurement noise. A way to improve the resolving power of seismic amplitudes is to perform inversion. The latter procedure can substantially reduce wavelet effects and hence deliver elastic parameters with a closer connection to petrophysical parameters than seismic amplitudes. In the case of post-stack seismic data, inversion yields estimates of acoustic impedance, whereas in the case of pre-stack seismic data, inversion yields estimates of bulk density, and compressional- and shear-wave velocities. Below, we analyze the relative merits of inversion to produce estimates of elastic parameters and indirectly of petrophysical variables.

8.1 Post-Stack Seismic Inversion.

Post-stack seismic inversion transforms the migrated seismic traces into time-domain variations of acoustic impedance. We inverted the simulated post-stack seismic data (contaminated with 10% additive, zero-mean Gaussian noise) via a nonlinear sparse-spike algorithm and the same Ricker wavelet used in the forward simulations. **Figure B-8.1** is intended to be a measure of the quality of the post-stack inversion along two segments of seismic traces intersecting either the shale background or the oil-saturated sand but not both. The cross-plots shown in **Figure B-8.1** are direct comparisons between the actual and inverted acoustic impedances at production time t_1=4 years. In a perfect case, all data should fall along a straight line of unity slope. In general, the two sets of acoustic impedances correlate very well, thereby giving credence to our inversion results.

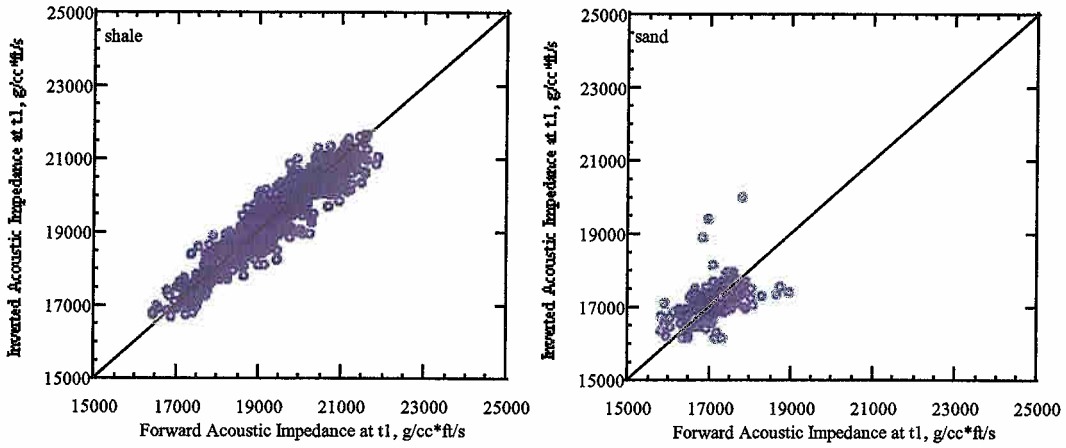

Figure B-8.1. Cross-plots of the original and inverted acoustic impedances at reservoir production time $=t_1=4$ years. The left panel only considers data sampled within the shale background, whereas the right panel only considers data sampled within the oil-producing sand.

Figure B-8.2 shows cross-sections in time of the inverted acoustic impedances along the center of the oil-saturated sand. In order to emphasize the role played by production time, the cross-sections shown in **Figure B-8.2** were constructed from the relative differences of acoustic impedance inverted at the production times of $t_1=4$ years, and $t_2=8$ years. For comparison, **Figure B-8.2** also displays a plot of the relative time difference of the distribution of water saturation along the same cross-section (left panel). Finally, and also for comparison purposes, the central panel in **Figure B-8.2** is a cross-section of the actual relative time differences of acoustic impedance. The inverted relative time differences of acoustic impedances are certainly a rather smooth version of the original values. This behavior is partly due to both the presence of noise in the inverted post-stack seismic data, and the limited frequency bandwidth of the Ricker wavelet. Qualitatively, however, it is rather clear from the plots shown in **Figure B-8.2** that acoustic impedances bear no clear and definite resemblance with the original spatial distribution of water saturation. A similar analysis shows that acoustic impedances do not portray a clear and definite resemblance with the spatial distributions of pore pressure either.

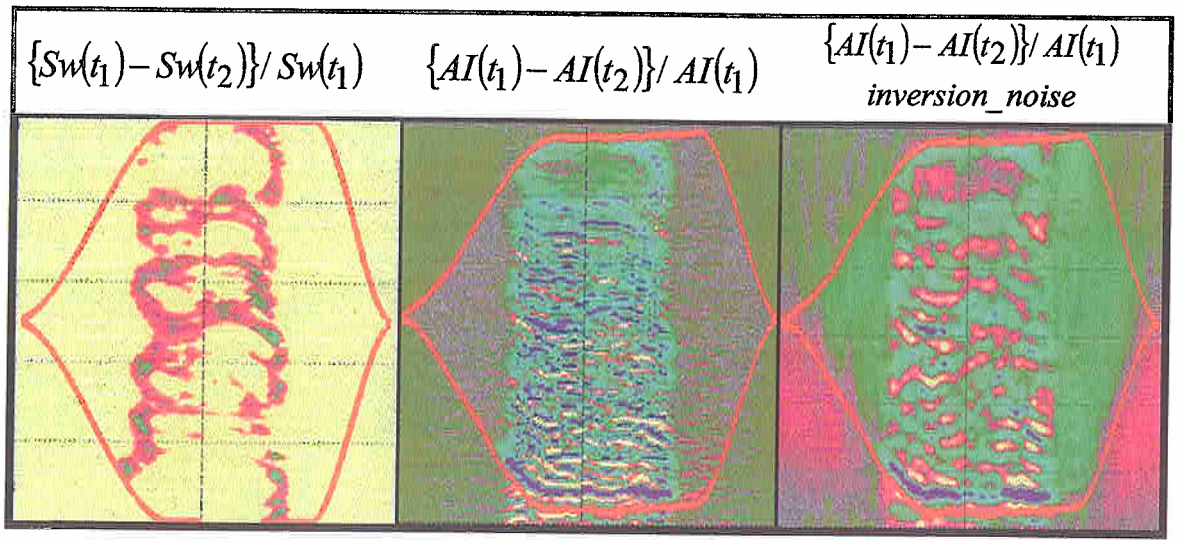

Figure B-8.2. Post-stack inversion results. Relative time differences of (a) water saturation, (b) acoustic impedance, and (c) inverted acoustic impedance, calculated from two time snapshots in the production life of the reservoir (t_2-t_1, where t_1 is 4 years and t_2 is 8 years after the onset of production.)

8.2 Pre-Stack Seismic Inversion.

In principle, pre-stack data provides considerably more flexibility than post-stack data to estimate petrophysical parameters from seismic amplitudes. This is due to fact that pre-stack seismic amplitudes are sensitive to bulk density, and compressional- and shear-wave velocities, whereas post-stack seismic data are only sensitive to P-wave acoustic impedances. It is expected, of course, that such an improved sensitivity would translate into better resolving and appraisal properties to infer distributions of petrophysical parameters. The study described in this section is intended to shed quantitative light to the resolving power of pre-stack seismic data. As in the case of the study of post-stack seismic data in the previous section, we choose to address our study of resolution by way of inversion.

Pre-stack seismic data were inverted using a nonlinear sparse-spike inversion algorithm that synthesizes data for near, mid, and far offsets to estimate values of bulk density, and compressional- and shear-wave velocity. The inversions described in this report were obtained from the simulated pre-stack seismic data contaminated with 10%, zero-mean Gaussian noise. Moreover, the inversions were performed with the same offset-dependent wavelets used in the forward simulations (see **Figure B-7.1**). **Figure B-**

8.3 is intended as a measure of the quality of the pre-stack inversion along two segments of seismic traces intersecting either the shale background or the oil-saturated sand but not both. The cross-plots shown in **Figure B-8.3** are direct comparisons between the actual and inverted compression-wave velocities at production time t_0=0 years. In a perfect case, all data should fall along a straight line of unity slope. In general, the two sets of compressional-wave velocities correlate very well, thereby giving credence to our inversion results. Similar comparison cross-plots were constructed for the inverted bulk density and shear-wave velocity. In these additional cases the correlation between the original and inverted variables was equally acceptable.

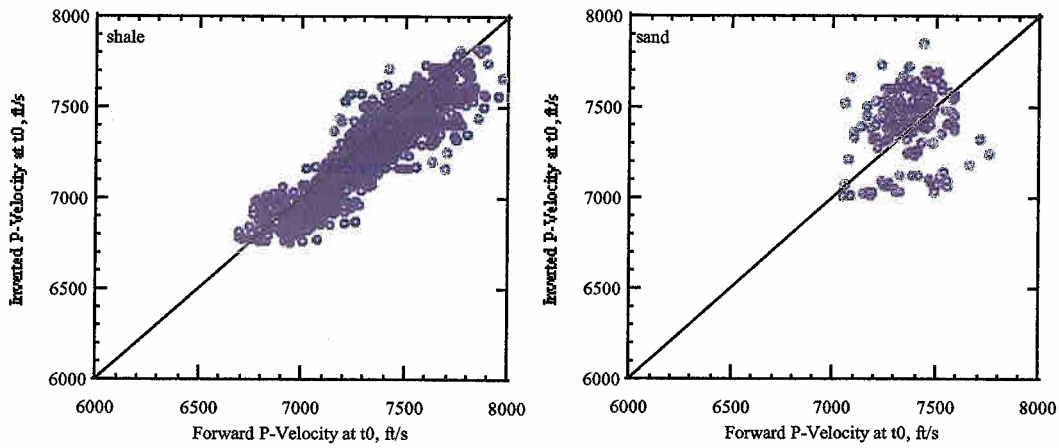

Figure B-8.3. Cross-plots of the original and inverted P-wave velocities at reservoir production time =t_0=0 years. P-wave velocities were inverted from pre-stack seismic data. The left panel only considers data sampled within the shale background, whereas the right panel only considers data sampled within the oil-producing sand.

Figure B-8.4 shows cross-sections in time of the inverted compressional-wave velocities along the center of the oil-saturated sand. In order to emphasize the role played by production time, the cross-sections shown in **Figure B-8.4** were constructed from the relative differences of compressional-wave velocity inverted at the production times of t_1=4 years, and t_2=8 years. For comparison, **Figure B-8.4** also displays a plot of the relative time difference of the distribution of water saturation along the same cross-section (left panel). Finally, and also for comparison purposes, the central panel in **Figure B-8.4** is a cross-section of the actual relative time differences of compressional-wave

velocity. The inverted relative time differences of compressional-wave velocity at best convey a blurred image of the original values. This behavior is partly due to both the presence of noise in the inverted pre-stack seismic data, and the limited frequency bandwidth of the pre-stack wavelets. However, compared with the acoustic impedance cross-sections shown in **Figure B-8.2**, compressional-wave velocities do bear a definite resemblance with the original spatial distribution of water saturation. A similar analysis shows that shear-wave velocities portray a clear and definite resemblance with the spatial distributions of pore pressure.

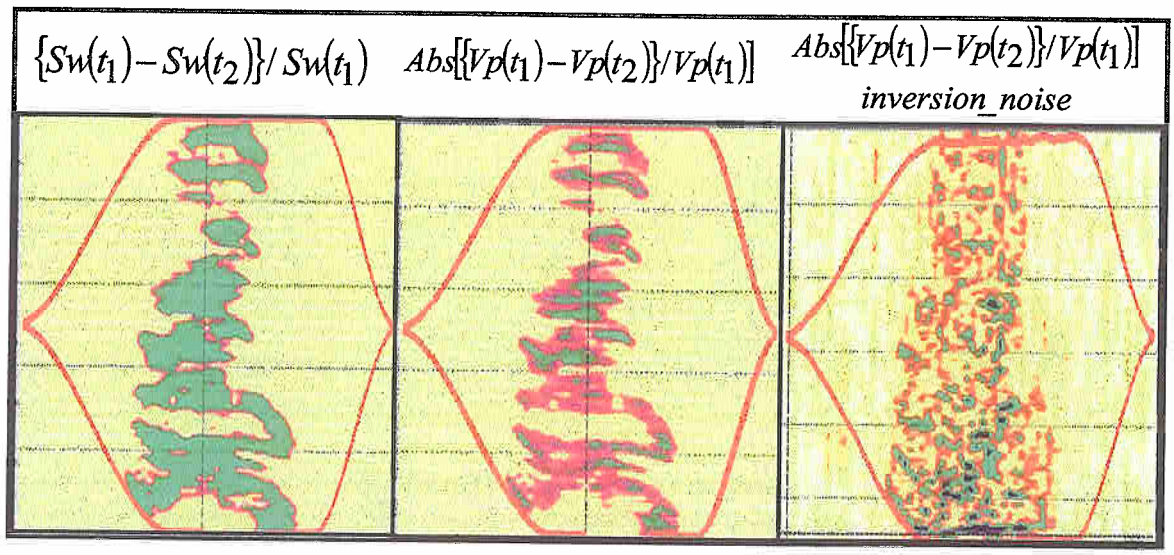

Figure B-8.4. Pre-stack inversion results. Relative time differences of (a) water saturation, (b) P-wave velocity, and (c) inverted P-wave velocity, calculated from two time snapshots in the production life of the reservoir (t_2-t_1, where t_1 is 4 years and t_2 is 8 years from the onset of production.)

8.3 Elastic Seismic Inversion.

Elastic inversion is a special case of pre-stack inversion. It makes use of only the far angle offset stacks and is particularly attractive when dealing with class III fluid-saturated sands (Rutherford and Williams, 1989). In our study, elastic logs input to the inversion were generated using the Knott-Zoeppritz equation. **Figure B-8.5** are cross-sections in time of the inverted elastic impedances along the center of the oil-saturated sand. These cross-sections were constructed from the relative differences of elastic impedance inverted at the production times of t_1=4 years, and t_2=8 years. For comparison,

Figure B-8.5 also shows a cross-section of the relative time difference of the distribution of water saturation along the same cross-section (left panel). Finally, the central panel in **Figure B-8.5** is a cross-section of the actual relative time differences of elastic impedance. The inverted relative time differences of elastic impedance are only a rough spatial average of the original values. Despite of this, however, elastic impedances bear a definite resemblance with the original spatial distribution of water saturation.

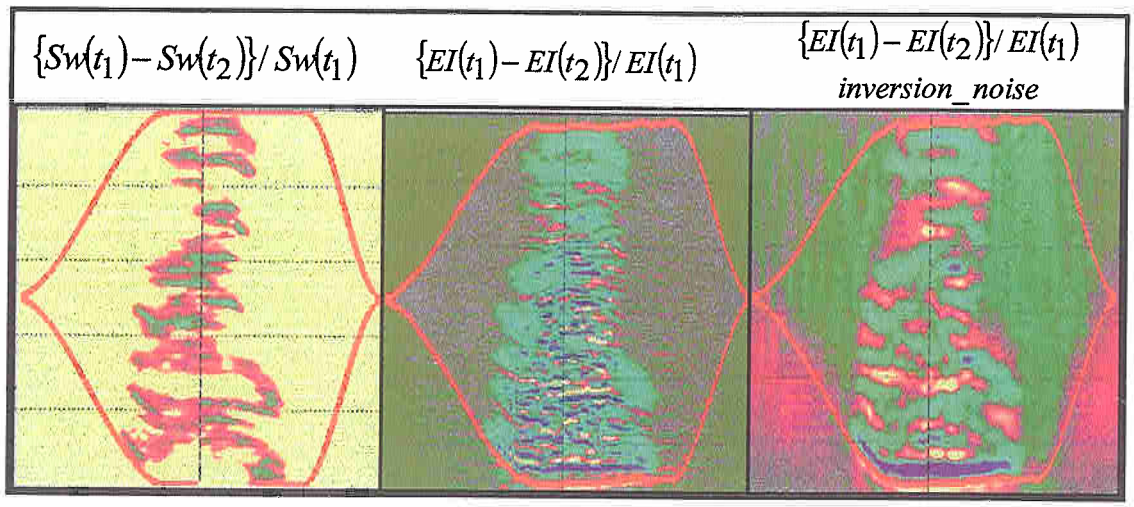

Figure B-8.5. Elastic inversion results. Relative time differences of (a) water saturation, (b) elastic impedance, and (c) inverted elastic impedance, calculated from two time snapshots in the production life of the reservoir (t_2-t_1, where t_1 is 4 years and t_2 is 8 years from the onset of production.)

9. SUMMARY OF PART B

Multiphase fluid flow parameters can have a sizable impact on fluid-saturation, pore pressure, and fluid pressure, and hence on the spatial distribution of elastic properties. We attempted to quantify the spatial resolution properties of 3D seismic data to time variations in petrophysical properties by way of inversion. Our study shows that the vertical resolution properties of seismic data provide only a smooth representation of the actual spatial distribution of petrophysical properties. Problems arise in thinly bedded reservoirs wherein the seismic data can only provide a rough spatial average of the actual distribution of petrophysical properties. We have shown that, even when not possessing

adequate vertical resolution, pre-stack seismic data embody more quantitative information that post-stack seismic data on the time-varying behavior of producing hydrocarbon reservoirs. We envision that an inversion strategy that honors both the high vertical resolution of well logs and the lateral resolution properties of pre-stack seismic data is the best strategy to detect and forecast the dynamic behavior of producing hydrocarbon reservoirs.

10. REFERENCES

Aki, K., and P. G. Richards (1980). Quantitative Seismology. W. H. Freeman and Company, San Francisco.

Biot, M.A. (1956). The theory of propagation of elastic waves in fluid-saturated solids, I lower frequency range, II higher frequency range. J. Acoust. Soc. Am., Vol 28, pp. 168-191.

Bourgoyne, A.T., Millheim, K.K., Chenevert, M.E., and F. S. Young (1991). Applied Drilling Engineering. SPE Textbook Series, Vol 2. Richardson, TX.

Castagna, J., and M. M. Backus (1993). Offset dependent reflectivity: Theory and Practice of AVO analysis, SEG publications.

Castagna, J.P., Batzle, M.L., and R.L. Eastwood (1985). Relationship between compressional wave and shear wave velocities in clastic silicate rocks. Geophysics, Vol. 50, No. 4, pp. 571-581.

Duffy , J. and R. D. Mindlin (1957). Stress-strain relations and vibrations of a granular medium. J. Appl. Mech. Vol. 24. pp. 585-593.

Engl, H. W. (1987). Discrepancy principles of Tikhonov regularization of ill-posed problems leading to optimal convergence rates: J. Optim. Theo. And Appl., **52**, pp. 209-215.

Elmore, W.C., and M. A. Heald (1969). Physics of Waves. Dover Publications, Inc. New York, NY.

Fryer, G. J., and L. N. Frazer (1984). Seismic waves in stratified anisotropic media, Geophys. J. R. Astr. Soc., 72, pp. 755-766.

Gassmann, F. (1951). Elastic waves through a packing of spheres. Geophysics, 16, pp. 673-685.

Geertsman, J. (1961). Velocity-log Interpretation: The Effect of Rock Bulk Compressibility. Soc. Pet. Eng., Vol. 1. pp. 235-248.

Geertsman, J. and D. C. Smith (1961). Some aspects of elastic wave propagation in fluid-saturated porous solids. Geophysics, Vol. 26. pp. 169-181.

Graebner, M. (1992). Plane-wave reflection and transmission coefficients for a transversely isotropic solid. Geophysics, 57, pp. 1512-1519.

Hamilton, E.L. (1971). Elastic properties of marine sediments. J. Geophys. Res., 76, pp. 579-601.

Hamilton, E.L. (1979). Vp/Vs and Poisson's ratios in marine sediments and rocks. J. Acoust. Soc. Am., Vol 66, No. 4, pp. 1093-1101.

Hornarpour, M., Koederitz, L.F., and A. H. Harvey (1982). Empirical equations for estimating two-phase relative permeability in consolidated rocks. Journal of Petroleum Technology, Vol. 34, pp. 2905-2908.

Ingber, L. (1989). Very fast simulated annealing, Math. Comput. Modeling, 12, pp. 967-993.

Kennett, B.L.N. (1984). Seismic Wave Propagation in Stratified Media, Cambridge University Press.

Kirkpatrick, S., Elatt, C. D., and M. P. Vecchi (1983). Optimization by simulated annealing: *Science*, 220, pp. 613-680.

Kormendi, F. and M. Dietrich (1991). Nonlinear waveform inversion of plane-wave seismograms in stratified elastic media. Geophysics, **56**, pp. 664-674.

Lake, L.W. (1989). Enhanced Oil Recovery. Prentice Hall. Englewood Cliffs, NJ.

McAuley, A. (1985). Prestack inversion with plane layer point source modeling. Geophysics, **50**, pp. 77-89.

Rutherford, S.R. and R. H. Williams (1989). Amplitude versus offset in gas sands. Geophysics, Vol. 54, No. 6. pp. 680-688.

Sen, M.K., and P.L. Stoffa (1991). Nonlinear one-dimensional seismic waveform inversion using simulated annealing. Geophysics, 56, pp. 1624-1638.

Sen, M.K., and P.L. Stoffa (1995). Global Optimization Methods in Geophysical Inversion. Elsevier Science Publishing Co.

Sen, M.K., and P.L. Stoffa (1996). Bayesian inference, Gibbs' sampler and uncertainty estimation in geophysical inversion. Geophys. Prosp., 44, pp. 313-350.

Sheriff, R.E. (1984). Encyclopedic Dictionary of Exploration Geophysics. Second Edition. Society of Exploration Geophysicists.

Simmons, J. L., and M. M. Backus (1996). Waveform based AVO inversion and AVO prediction-error. Geophysics, 61, pp. 1575-1588.

Smith, G. C., and P. M. Gidlow (1987). Weighted stack for rock property estimation and detection of gas. Geophys. Prosp., 35, pp. 993-1014.

Stoffa, P. L., Diebold, J. B., and P. Buhl (1982). Velocity analysis for wide aperture seismic data. Geophys. Prosp., **30**, pp. 25-57.

Taner, M. T., and F. Koehler (1969). Velocity spectra - digital computer derivation and applications of velocity functions. Geophysics, **34**, pp. 859-881.

Tiab, D. and E. C. Donaldson (1996). Petrophysics: Theory and Practice of Measuring Reservoir Rock and Fluid Transport Properties. Gulf Publishing Company, Houston, TX.

Tosaya, M.N., and A. Nur (1982). Effects of diagenesis and clays on compressional velocities in rocks. Geophysics, Res. Lett., 9, pp. 5-8.

Varela, O. J., Torres-Verdín, C., Sen, M.K., and J. Roy (2001). Synthetic studies for the efficient quantitative integration of time-lapse reservoir production data, geological information, well logs, and pre- and post-stack 3D seismic data. SEG Development and Production Forum, Taos, New Mexico, June 24-29.

Varela, O.J. (2002) Pre-stack Stochastic Seismic Inversion to Improve Reservoir Simulation Forecast. PhD Dissertation in progress. The University of Texas at Austin.

White, J.E. (1983). Underground Sound: Application of Seismic Waves. Elsevier, New York, NY.

Xia, G., M.K. Sen, and P.L. Stoffa, 1998, 1-D elastic waveform inversion: A divide-and-conquer approach. Geophysics, 63, pp. 1670-1684.

Xia, G., M.K. Sen, and P.L. Stoffa, 1999, Mapping of elastic properties of gas hydrates in the Carolina Trough by waveform inversion. Geophysics, 65, pp. 735-744.